Argonne
NATIONAL LABORATORY

ANL/09-32

Cracking Behavior and Microstructure of Austenitic Stainless Steels and Alloy 690 Irradiated in BOR-60 Reactor, Phase I

Nuclear Engineering Division

ANL/09-32

Cracking Behavior and Microstructure of Austenitic Stainless Steels and Alloy 690 Irradiated in BOR-60 Reactor, Phase I

prepared by
Y. Chen, O.K. Chopra, W.K. Soppet, and W.J. Shack
Argonne National Laboratory

Y. Yang and T. Allen
University of Wisconsin-Madison

A.S. Rao, NRC Project Manager

February 2007

This page is intentionally left blank.

Abstract

Cracking behavior of stainless steels specimens irradiated in the BOR-60 at about 320°C is studied. The primary objective of this research is to improve the mechanistic understanding of irradiation-assisted stress corrosion cracking (IASCC) of core internal components under conditions relevant to pressurized water reactors. The current report covers several baseline tests in air, a comparison study in high-dissolved-oxygen environment, and TEM characterization of irradiation defect structure.

Slow strain rate tensile (SSRT) tests were conducted in air and in high-dissolved-oxygen (DO) water with selected 5- and 10-dpa specimens. The results in high-DO water were compared with those from earlier tests with identical materials irradiated in the Halden reactor to a similar dose. The SSRT tests produced similar results among different materials irradiated in the Halden and BOR-60 reactors. However, the post-irradiation strength for the BOR-60 specimens was consistently lower than that of the corresponding Halden specimens. The elongation of the BOR-60 specimens was also greater than that of their Halden specimens. Intergranular cracking in high-DO water was consistent for most of the tested materials in the Halden and BOR-60 irradiations. Nonetheless, the BOR-60 irradiation was somewhat less effective in stimulating IG fracture among the tested materials.

Microstructural characterization was also carried out using transmission electron microscopy on selected BOR-60 specimens irradiated to ≈25 dpa. No voids were observed in irradiated austenitic stainless steels and cast stainless steels, while a few voids were found in base and grain-boundary-engineered Alloy 690. All the irradiated microstructures were dominated by a high density of Frank loops, which varied in mean size and density for different alloys.

This page is intentionally left blank.

Contents

Figures

Tables

Executive Summary

Irradiation-assisted stress corrosion cracking (IASCC) and irradiation microstructure of austenitic stainless steels (SSs) in pressured water reactors (PWRs) are the subjects of investigation for the current study. Various core internal components of commercial and test PWRs become susceptible to cracking after extended neutron exposure. Although it is well understood that radiation-induced microstructural and microchemical changes are the root cause of poor cracking resistance, the exact cracking mechanism operating under PWR environment is not clear at present. The database for PWR internals is still limited, and the key metallurgical variables for IASCC in PWR environment have not been identified. A better mechanistic understanding of cracking of SSs is crucial not only for developing predictive models but also for establishing possible countermeasures to mitigate IASCC for PWR internals. The objective of the present study is to evaluate the cracking susceptibility of core internal materials and to advance the current understanding of cracking mechanisms in PWR environment. The present report summarizes the preliminary results of the BOR-60 slow strain rate tensile (SSRT) tests in air and in high dissolved-oxygen (DO) water, comparison between the BOR-60 and Halden SSRT tests, and transmission-electron-microscope (TEM) examination of 20-dpa specimens.

Slow strain rate tensile specimens and TEM disks were irradiated in the BOR-60 reactor, a sodium-cooled fast breeder reactor, to various neutron fluences at about 320°C. All tensile specimens and most of TEM disks were exposed to sodium coolant during irradiation. One of TEM capsules was irradiated at the same temperature in a helium-sealed capsule. The damage rate of the BOR-60 irradiation was about 10^{-6} dpa/s.

A total of 11 SSRT tests were conducted on the 5-dpa and 10-dpa Type 304 and 316 SSs specimens in air and in high-DO water. All tests were performed at a strain rate of 7.4×10^{-7} 1/s. Significant irradiation hardening and loss of ductility were observed in all irradiated specimens regardless of test environment. No strain hardening can be seen at 5 and 10 dpa levels for the tested specimens. Strain softening behavior is more evident for cold-worked 10-dpa specimens. After the SSRT tests, fractographic examination was performed on the specimens tested in high-DO water. Significant amount of intergranular (IG) cracking was observed in the materials with high sulfur and high oxygen contents.

The BOR-60 SSRT tests were compared with previous tests conducted on the specimens irradiated in the Halden reactor (a heavy water test reactor) to a similar dose level. It was found that the post-irradiation strength for the BOR-60 specimens was consistently lower than that of the corresponding Halden specimens. The elongation of the BOR-60 specimens was also greater than that of the Halden specimens. In general, intergranular cracking behavior in high-DO water was consistent in the Halden and BOR-60 irradiations for most of the tested materials. However, it appears that the BOR-60 irradiation is somewhat less effective in stimulating IG fracture.

Irradiation microstructure was examined using a TEM on several BOR-60 specimens irradiated to ≈25 dpa. The dominant irradiation defects in these materials were Frank loops. The measured density and size of Frank loops are consistent with what reported in the literature. Voids and cavities were examined carefully in these SSs using through-focus technique under a bright-field kinematical condition. No void was observed in austenitic SSs and cast SSs, while a few voids were found in base and grain-boundary-engineered Alloy 690. It appears that void swelling is negligible for these BOR-60 specimens.

This page is intentionally left blank.

Acknowledgments

The authors would like to thank Dr. Raj Pathania and Dr. Peter Scott for arranging irradiations through the Cooperative IASCC Research (CIR) program in the BOR-60 reactor. The authors would also like to thank Dr. Regis P. Shogan of Westinghouse for transferring the irradiated specimens from Russia to Argonne National Laboratory. L. A. Knoblich, E. E. Gruber, R. Clark, and E. J. Listwan are acknowledged for their contributions to the experimental effort. We are also grateful to W. H. Cullen, Jr., R. Tregoning and S. Crane for many helpful discussions and suggestions. This work is sponsored by the Office of Nuclear Regulatory Research, U.S. Nuclear Regulatory Commission, under Job Code Y6388; Program Manager: A. S. Rao.

This page is intentionally left blank.

Abbreviations

BF	Bright Field
BWR	Boiling Water Reactor
CW	Cold Worked
DF	Dark Field
dpa	displacement per atom
DO	Dissolved Oxygen
EFPY	Effective Full Power Years
ECP	Electrochemical Potential
EOL	End of Life
GBE	Grain Boundary Engineered
HP	High Purity
IASCC	Irradiation-Assisted Stress Corrosion Cracking
IG	Intergranular
IML	Irradiated materials Laboratory
LWR	Light Water Reactor
PWR	Pressurized Water Reactor
RIAR	Research Institute of Atomic Reactor
RIS	Radiation-Induced Segregation
SA	Solution Annealed
SAD	Selected area diffraction
SEM	Scanning Electron Microscopy
SHE	Standard Hydrogen Electrode
SS	Stainless Steel
SSRT	Slow Strain Rate Tensile
TE	Total Elongation
TEM	Transmission Electron Microscopy
TG	Transgranular
UE	Uniform Elongation
UTS	Ultimate Tensile Strength
WBDF	Weak Beam Dark Field
WW	Warm Worked
YS	Yield Strength

This page is intentionally left blank.

1 Introduction

Irradiation-assisted stress corrosion cracking (IASCC) has been observed in various core internal components of commercial and test pressurized water reactors (PWRs).[1-6] Failures of the fuel cladding, control rod cladding, and core baffle bolts in PWRs have revealed intergranular (IG) fracture similar to the failure observed in the core internals of boiling water reactors (BWRs).[3,4,6] However, because of the low corrosion potential, the typical "threshold" neutron dose for IASCC in PWRs is about one order of magnitude higher than that in BWRs with normal water chemistry.[5] Also, chromium depletion at grain boundaries is considered as less critical for IASCC sensitivity in PWRs than in BWRs. The high irradiation "threshold" for the occurrence of IASCC implies that radiation-induced embrittlement may play a more important role in the cracking of PWR internals. At present, the database for PWR internals is still very limited, and the key metallurgical variables for IASCC in the PWR environment have not been clearly identified. Whether or not the irradiation embrittlement alone is sufficient to explain the IG cracking in PWR core components needs to be further investigated. Although radiation-induced microstructural and microchemical changes are known to be the root cause of IASCC, the exact mechanism operating under the PWR environment is not clear. A better mechanistic understanding of cracking in the PWR environment is crucial not only for establishing possible countermeasures to mitigate IASCC but also for developing predictive and regulatory methodology.

Void swelling is another issue associated with the high dose level at the end of life (EOL) in PWRs. In the past, the volumetric instability caused by swelling was mainly a concern in fast breeder reactors and fusion systems. The peak temperature of void swelling was found to be around 550-600°C for austenitic stainless steels (SSs).[7,8,9] The void swelling at temperatures relevant to light water reactors (LWRs) is insignificant and was not considered a problem for either PWRs or BWRs within their service life. More recently, Garner and Toloczko[10] pointed out that the predicted void swelling based on the fast breeder reactor data may not properly represent the situation in LWRs. The lower damage rate ($\sim 10^{-7}$ dpa/s) in LWRs may reduce the incubation limit and shift the peak swelling temperature towards the low temperature region. A small amount of void swelling (< 1%) was indeed observed in a Russian austenitic steel irradiated at PWR-relevant dose rates and temperatures.[11] Combined with the apprehension that temperatures up to 450°C might occur due to γ-radiation heating in the thick section of components, void swelling is a possible concern for the EOL dose level of PWRs. This concern triggered a recent literature survey of void swelling under PWR relevant conditions.[12] With very limited data on decommissioned components from PWRs, the study confirmed the previous conclusion that void swelling is relatively low under PWR conditions. However, because of the significance of volumetric stability and the possible extreme brittleness associated with voids,[13] void swelling of austenitic SSs needs to be closely examined under dose and temperature conditions relevant for PWRs.

Another issue to be addressed in the current study is the influence of irradiation conditions (neutron spectrum and irradiation temperature) on IASCC susceptibility. It has been confirmed that "persistent effects" induced by irradiation are responsible for IASCC.[2,14] Thus, irradiation conditions that influence the microstructural and microchemical evolution must impact the IASCC susceptibility. Since radiation damage produced by various irradiation sources are different, displacement per atom (dpa) that incorporates the energy dependent response of materials is a dose unit often used to characterize the defect generation under irradiation.[15,16] Norgett, Robinson and Torrens developed a widely acceptable method for calculating the dpa in irradiated metals ("NRT model").[17] However, irradiation effects (such as IASCC) are caused by surviving point defects rather than the point defects resulting directly from the cascade damage. The defect survival rate for a low energy cascade from thermal neutrons is higher than that caused by fast neutrons. Meanwhile, the defect survival rate is lower at higher irradiation temperature. Thus, the dose measured by dpa is only a first approximation for the irradiation exposure.

The influence of irradiation conditions on IASCC susceptibility shall be further analyzed, and the possible connections between the radiation-induced microstructural and microchemical changes and IASCC behavior need to be explored.

A study to evaluate the IASCC susceptibility of austenitic SSs as a function of the fluence, material chemistry, and cold-work in the PWR environment is in progress at Argonne National Laboratory. This report provides some preliminary results on slow strain rate tensile (SSRT) tests in air and in high-dissolved-oxygen (DO) water for specimens irradiated in the BOR-60 reactor. By comparing the IASCC susceptibility of identical materials irradiated in the BOR-60 reactor and the Halden reactor in Norway, the possible influence of irradiation conditions on IASCC is investigated. The microstructural examinations on void swelling and irradiation defects in austenitic SSs at PWR-relevant doses and temperatures are also summarized in this report.

2 Experimental

2.1 BOR60 Irradiation

Irradiation experiments were conducted in the BOR-60 reactor, a sodium-cooled fast breeder reactor located in the Research Institute of Atomic Reactor (RIAR), Dimitrovgrad, Russia. Various austenitic SSs and Alloy 690 were included in this irradiation campaign. Table 1 provides the chemical compositions of the materials. Both SSRT specimens (Fig. 1) and transmission-electron-microscope (TEM) disks (3 mm in diameter) were irradiated to approximate doses of 5, 10, 20 and 40 dpa during Boris-6 and -7 irradiation experiments. The tensile specimens were separated in bundles (four specimens in each bundle) and were in contact with the sodium coolant during irradiation. The TEM disks were contained in four weeper capsules and one helium-tight capsule, as shown in Fig. 2. The TEM disks in the weeper capsules were in contact with sodium during irradiation.

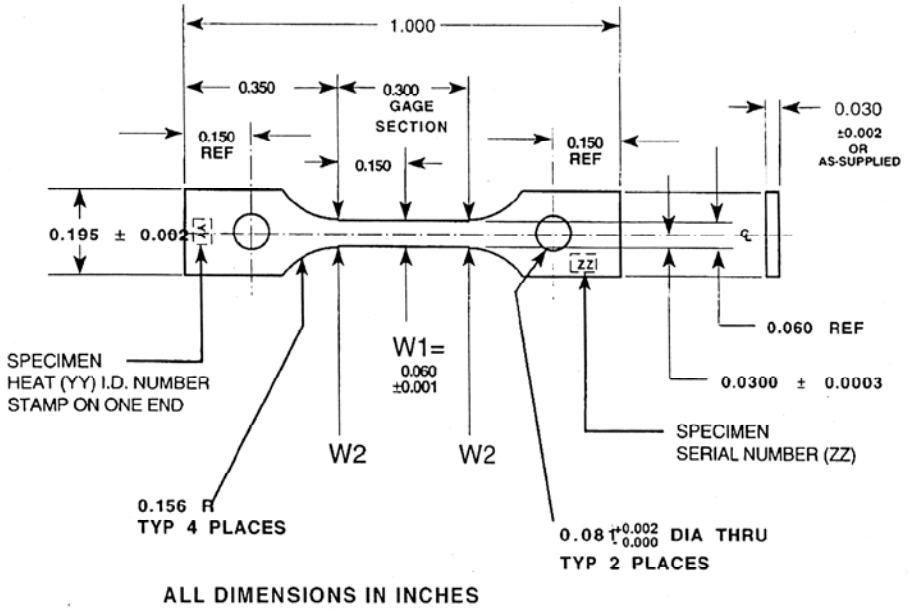

Figure 1. Schematic of BOR-60 flat SSRT specimen (1 inch = 25.4 mm).

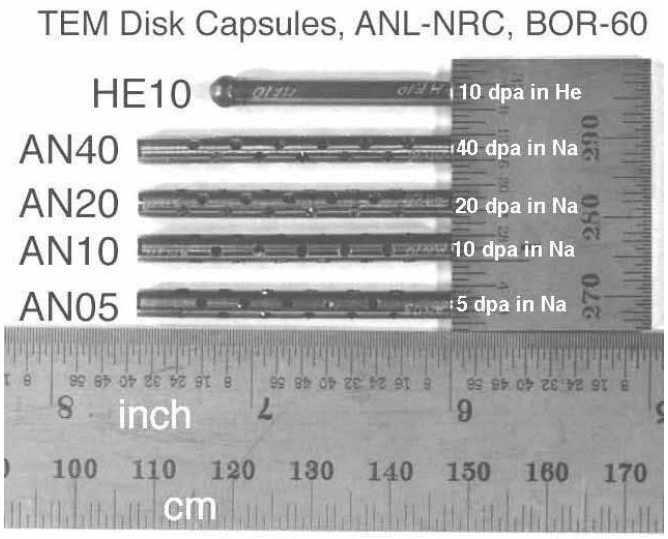

Figure 2.
TEM capsules irradiated in the BOR-60 reactor.

Specimens from the Boris-6 irradiation, which included 8 irradiation sub-cycles and several shut-down periods, were used in this study. The irradiation was conducted in the fifth row of the core of the BOR-60 reactor. Neutron fluence was monitored by five dosimeters loaded in the central channel of the irradiation rig and in baskets with the specimens. The analyses of dosimeters were carried out by RIAR after irradiation.[18] The irradiation temperature was controlled by monitoring the inlet and outlet sodium temperatures, which were kept at ≈315 and 325°C, respectively; Mg-Zn eutectic thermal monitors were also placed among specimens in several baskets to ensure that the irradiation temperature was below 343°C.

The Boris-6 irradiation specimens were discharged at different times between 2001 and 2003 according to the target doses. All specimens were first cleaned of residual sodium and then transferred to Argonne via Studsvik and Westinghouse in 2005. In total, 48 tensile specimens and 166 TEM disks were irradiated during the Boris-6 cycle, as listed in Table 2. The actual doses received by individual specimens are given in Table 3.

Table 1. Materials irradiated in BOR-60 reactor (wt.%).

Material Type[a]	Heat ID	Composition (wt.%)								
		Ni	Si	P	S	Mn	C	N	Cr	Other Elements [b]
347 SA	316642	10.81	0.29	0.023	0.014	1.56	0.030	0.021	18.06	Nb 0.60, Mo 0.29, Cu 0.09
347 CW	316642CW	10.81	0.29	0.023	0.014	1.56	0.030	0.021	18.06	Nb 0.60, Mo 0.29, Cu 0.09
304 SA	2333	8.5	0.65	0.031	0.029	1.38	0.035	0.068	18.30	Mo 0.37
304 CW	2333CW	8.5	0.65	0.031	0.029	1.38	0.035	0.068	18.30	Mo 0.37
316 LN SA	623	12.20	0.70	0.007	0.002	0.97	0.019	0.103	17.23	Mo 2.38, Cu 0.21
316 LN-Ti SA	625	12.30	0.72	0.007	0.002	0.92	0.012	0.064	17.25	Mo 2.38, Ti 0.027, Cu 0.21
316 SA	C21	10.24	0.51	0.034	0.001	1.19	0.060	0.020	16.28	Mo 2.08, B<0.001
316 CW	C21 CW	10.24	0.51	0.034	0.001	1.19	0.060	0.020	16.28	Mo 2.08, B<0.001
316 WW	C21 WW	10.24	0.51	0.034	0.001	1.19	0.060	0.020	16.28	Mo 2.08, B<0.001
CF-3 cast SS	52	9.40	0.92	0.012	0.005	0.57	0.009	0.052	19.49	Mo 0.35, δ 13.5%
CF-8 cast SS	59	9.34	1.08	0.008	0.007	0.60	0.062	0.045	20.33	Mo 0.32, δ 13.5%
CF-3 cast SS	69	8.59	1.13	0.015	0.005	0.63	0.023	0.028	20.18	Mo 0.34, δ 23.6%
CF-8 cast SS	68	8.08	1.07	0.021	0.014	0.64	0.063	0.062	20.64	Mo 0.31, δ 23.4%
304 SA	C1	8.12	0.50	0.038	0.002	1.00	0.060	0.060	18.11	B 0.001
304 SA	C9	8.75	0.39	0.013	0.013	1.72	0.062	0.065	18.48	B <0.001
304 SA	C12	8.23	0.47	0.018	0.002	1.00	0.060	0.070	18.43	B <0.001
304 CW	C1 CW	8.12	0.50	0.038	0.002	1.00	0.060	0.060	18.11	B 0.001
304 CW	C12 CW	8.23	0.47	0.018	0.002	1.00	0.060	0.070	18.43	B <0.001
304 GBE	304 GBE	8.43	0.46	0.014	0.003	1.54	0.065	0.088	18.38	Mo 0.51, Co 0.22
316 GBE	316 GBE	11.12	0.57	0.011	0.022	1.85	0.070	0.056	16.57	Mo 2.27, Co 0.10
690 GBE	690 GBE	59.40	0.30	-	0.003	0.42	0.010	-	29.10	Fe 10.26
304 BASE	304 BASE	8.46	0.41	0.013	0.014	1.56	0.065	0.086	18.32	Mo 0.36, Co 0.12
316 BASE	316 BASE	10.30	0.43	0.013	0.020	1.53	0.055	0.054	16.42	Mo 2.19, Co 0.10
690 BASE	690 BASE	61.49	0.05	-	<0.01	0.15	0.030	-	29.24	Fe 9.02
HP 304L SA	945	9.03	0.03	<0.005	0.005	1.11	0.005	0.003	19.21	O 0.047, Mo <0.005
HP 304L SA	1327	9.54	0.01	0.001	0.002	1.12	0.006	<0.001	19.71	O 0.008, Mo 0.02
304L SA	C3	8.91	0.46	0.019	0.004	1.81	0.016	0.083	18.55	B< 0.001
304L CW	C3 CW	8.91	0.46	0.019	0.004	1.81	0.016	0.083	18.55	B< 0.001
304-like alloy	L5	9.66	0.90	0.113	0.028	0.47	0.006	0.033	21.00	B<0.001

[a]SA = solution annealed; CW = cold worked; WW = warm worked at 400°C; SS = stainless steel; GBE = grain boundary engineered; BASE = base heat for GBE modification; HP = high purity.

[b]δ = ferrite content.

Table 2. Available specimens from Boris-6 and -7 irradiations.

Material Type [a]	Heat ID	SSRT Specimens [b]			TEM Disks [b]				
		5 dpa	10 dpa	40 dpa	5 dpa	10 dpa	10 dpa (He cap.)	20 dpa	40 dpa
347 SA	316642	1	2	2	2	1	1	1	2
347 CW	316642CW	2	2	2	2	1	1	2	2
ABB 304 SA	2333	-	2	-	2	1	1	2	2
ABB 304 CW	2333 CW	-	2	1	2	1	1	2	2
316LN SA	623	1	2	-	2	1	1	2	2
316LN-Ti SA	625	1	2	3	2	1	1	2	2
316 SA	C21	1	3	2	2	1	1	2	2
316 CW	C21 CW	2	3	1	2	1	1	1	2
316 WW	C21 WW	-	2	2	2	2	-	2	2
CF-3 cast	52	-	2	-	2	1	1	2	2
CF-8 cast	59	-	2	-	2	2	-	2	2
CF-3 cast	69	-	-	2	2	1	-	1	2
CF-8 cast	68	-	-	2	2	2	-	2	2
304 SA, low S	C1	1	2	-	2	1	1	2	2
304 SA, high S	C9	1	2	-	2	1	1	2	2
304 SA, low S	C12	1	2	-	2	1	1	2	2
304 CW, low S	C1 CW	1	2	-	2	1	1	2	2
304 CW, low S	C12 CW	1	2	1	2	1	1	2	2
304 GBE	304 GBE	1	2	1	2	1	1	2	2
316 GBE	316 GBE	1	2	1	2	1	1	2	2
690 GBE	690 GBE	1	2	1	2	1	1	2	2
304 BASE	304 BASE	1	2	-	2	1	1	2	2
316 BASE	316 BASE	1	2	-	2	2	-	2	2
690 BASE	690 BASE	1	2	-	2	2	-	2	2
HP 304L SA, high O	945	1	2	1	2	1	1	2	2
HP 304L SA, low O	1327	1	2	3	2	2	2	2	2
304L SA	C3	1	2	-	-	-	-	-	-
304L CW	C3 CW	1	2	1	2	1	1	2	2
304-like alloy	L5	1	2	3	2	1	1	2	2
	Total	24	56	29	56	34	23	53	56

[a] SA = solution annealed; CW = cold worked at room temperature; WW = warm worked at 400°C; GBE = grain boundary engineered; BASE = base heat for GBE modification; HP = high purity.

[b] Doses are targeted dose. The specimens tested in this study are highlighted.

Table 3. Displacement damage dose for specimens irradiated in Boris-6 irradiation cycle.

Specimen Type	Capsule ID / Bundle ID	Specimen IDs	Dose (dpa)
TEM	AN 05	-	5.5
	AN 10	-	10.2
	AN 20	-	24.5
	HE 10	-	11.8
SSRT	D1-1/B3-1	D1-1, D2-1, D2-2, B3-1	5.5
	A5-1/E1-1	A5-1, A6-1, B8-1, E1-1	5.5
	B4-1/B6-2	B4-1, B5-1, B6-1, B6-2	5.5
	A7-1/A8-1	A7-1, B9-1, E2-1, A8-1	4.8
	A1-1/A4-1	A1-1, A2-1, A3-1, A4-1	4.8
	A9-1/A12-1	A9-1, A10-1, A11-1, A12-1	4.8
	D1-2/D2-4	D1-2, D1-3, D2-3, D2-4	10.2
	B1-1/B2-2	B1-1, B1-2, B2-1, B2-2	10.2
	B3-2/B4-3	B3-2, B3-3, B4-2, B4-3	11.8
	B5-2/B6-3	B5-2, B5-3, B5-4, B6-3	11.8
	B6-4/B7-2	B6-4, B6-5, B7-1, B7-2	10.4
	C1-1/C2-2	C1-1, C1-2, C2-1, C2-2	10.4

2.2 Slow Strain Rate Tensile Tests

The SSRT tests on BOR-60 specimens were conducted in a test facility that is located in hot cell #1 of the Irradiated Materials Laboratory (IML) at Argonne. This testing facility is equipped with a worm gear actuator, a set of gear reducers, and a variable speed motor with control. The high-purity water environment was provided by the recirculation loop shown schematically in Fig. 3. The water loop consists of a storage tank, 0.2 micron filter, high-pressure pump, regenerative heat exchanger, autoclave preheater, test autoclave, electrochemical potential (ECP) cell preheater, ECP cell, air-cooled heat exchanger, Mity Mite^{TM} back-pressure regulator, two ion-exchange cartridges, another 0.2 micron filter, and return line to the storage tank. The high-pressure portion of the system extends from the high-pressure pump (item 10) to the back-pressure regulator (item 27). Over-pressurization of the loop is prevented by a rupture disk (set at 2300 psig or 15.8 MPa) installed upstream of the high-pressure pump.

1. Cover-gas supply tank
2. Two-stage high-pressure regulator
3. Low-pressure regulator
4. Compound vacuum & pressure gauge
5. Feed water storage tank
6. Sparger
7. Tank water sample port
8. Solenoid valve
9. 0.2 micro filter
10. High-pressure pump
11. Rupture disk
12. Check valve
13. High-pressure gauge
14. Heat exchanger
15. Autoclave preheater
16. Tube autoclave
17. Thermocouple well
18. ECP cell preheater
19. Preheater thermocouple
20. ECP cell
21. ECP cell thermocouple
22. SS electrode
23. Standard reference electrode
24. Platinum electrode
25. Heat exchanger
26. Cooling fan
27. Back-pressure regulator
28. Outlet vent port
29. Loop water sampling port (not use)
29B. Loop water sampling port (new)
30. Ion exchange bed
31. 2nd ion exchange bed
32. 0.2 micron filter
33. Feed water fill port
34. Recirculation pump
35. Check valve
36. Pressure relief valve to tank
37. Check valve
38. Bypass pressure relief valve

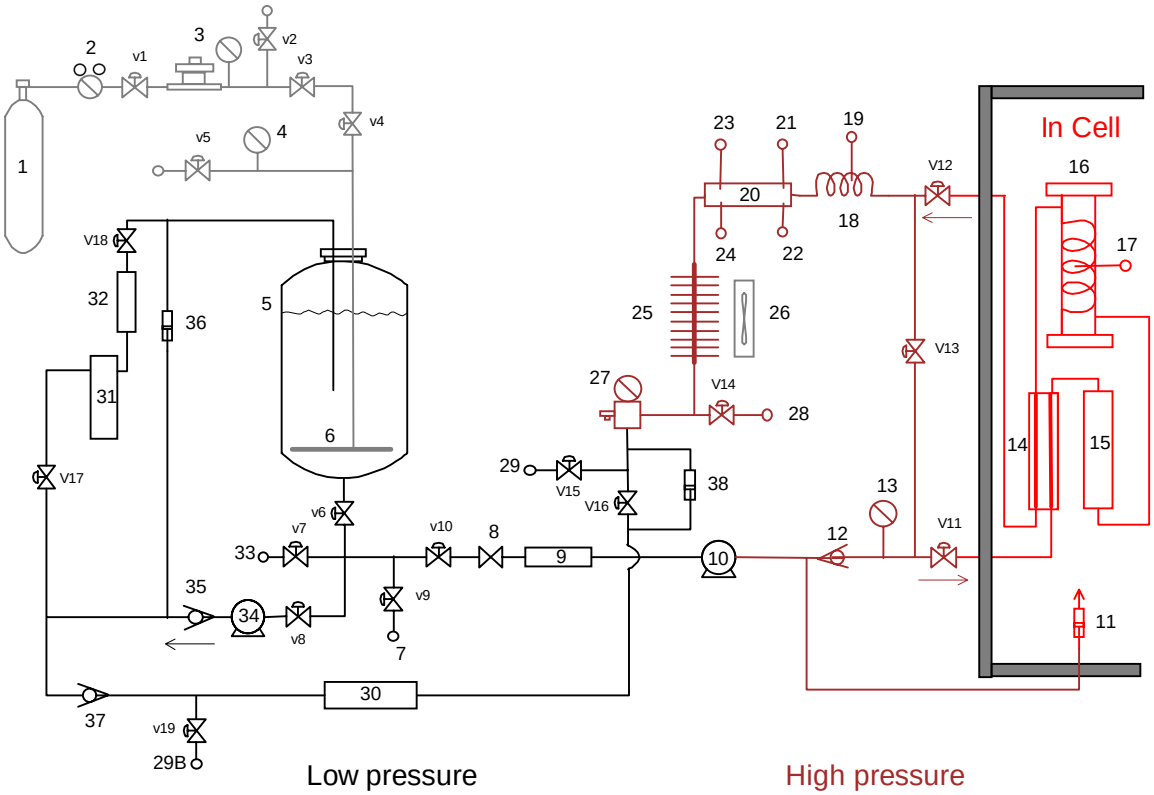

Figure 3. Schematic diagram of the recirculation water system.

The experimental effort for the BOR-60 SSRT tests focused on determining the possible effect of irradiation condition. The SSRT tests were performed in air at ≈320°C or in high-purity water at ≈289°C. The specimens selected for this study are highlighted in Table 2. For air tests, a less than 2°C temperature gradient was estimated along the gauge section of the SSRT specimen, and the test temperature was 320±5°C. For the water tests, no temperature gradient was expected within the gauge section, and the temperature was 289±2°C. The DO content for all water tests was about ≈8 ppm. The system pressure was maintained at ≈9.31 MPa (≈1350 psig) during the tests in water. The conductivity and pH of water at room temperature were maintained at 0.06-0.10 μS/cm and 6.4-7.2, respectively. The flow rate of the system was 15-30 ml/min, and water samples were taken periodically to monitor the resistivity, pH, and DO level in the effluent. The ECP of a platinum (Pt) electrode (item 24 in Fig. 3) and a SS sample (item 22) located downstream from the tube autoclave (item 16) was monitored continuously during the test. The strain rate during the SSRT tests was held constant at ≈7.4 x 10^{-7} s^{-1}.

Because of the small dimension of the irradiated BOR-60 specimens, extreme caution was required for installing them remotely. To avoid bending or twisting during installation, a special sample grip system was designed (Fig. 4). The sample grip includes two guiding rods that insert into the holes in both top and bottom halves to maintain the proper alignment during the test. The specimen was centered between two loading pins on the sample grip. After the two cover clips are tightened, the specimen can only be loaded under tension and is protected from bending or twisting. The sample grip was then inserted into the tube autoclave and engaged with pull rods from both ends. The assembled autoclave was hung on the test frame without the lower pin in place to keep a stress-free condition until the desired temperature and pressure were achieved. Also, the specimen was soaked in the test environment [289°C, ≈9.3 MPa (552°F, ≈1350 psi)] for about 24 hours under a tensile stress less than ≈140 MPa (≈20.3 ksi) prior to the SSRT test.

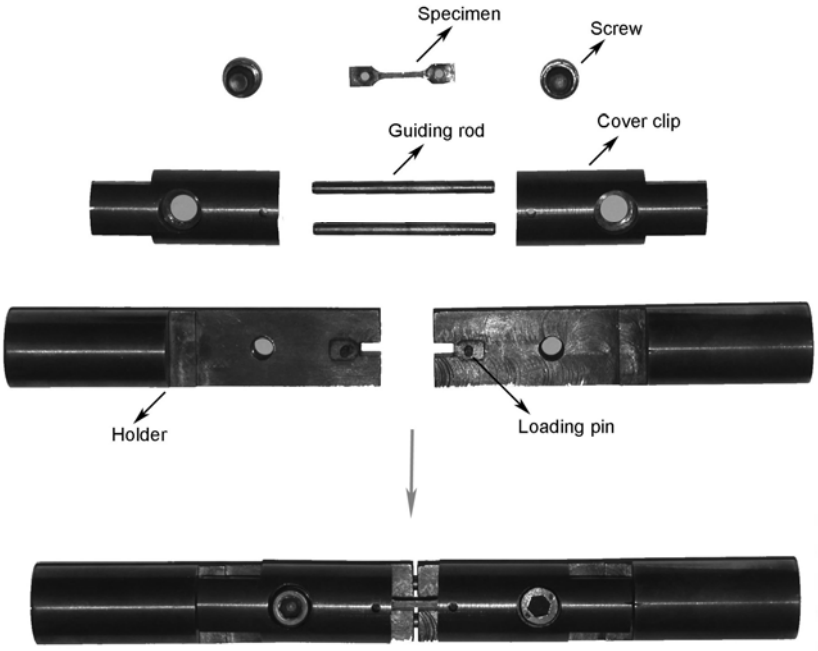

Figure 4. SSRT sample grip for BOR-60 specimen.

2.3 Fractographic Examination

After the SSRT test, the fractured specimens were cleaned to remove loose contamination. The decontaminated specimens were then transferred to a scanning electronic microscopy (SEM) facility on-site for fractographic examination. Both the fracture surface and gauge surface of the tested specimens were observed and documented. To minimize the radiation exposure, the shoulder of a tested specimen was removed prior to cleaning. The SEM used in this study was a Hitachi S-300N variable pressure microscope located in a radiological control area. The secondary electron image at 30-kV acceleration voltage with 25-mm work distance was used for most of the observations.

2.4 Irradiation Microstructure Characterization

Eleven selected TEM disks of austenitic SSs and Alloy 690 irradiated to ≈24.5 dpa at ≈320°C were examined in this study. The heat IDs are 2333CW, C9, C12, 623, 945, 690 BASE, 690 GBE, 52, 59 and 68. Their composition is given in Table 1. The as-irradiated TEM specimens were prepared using a two-step electropolishing procedure. The irradiated microstructure was characterized with a JOEL-100CX TEM located in a radiological control area at Argonne, and control nonirradiated specimens were examined with a JEOL 200CX or a Philips CM 200CM TEM at the University of Wisconsin-Madison.

2.4.1 Sample Preparation

A single-vertical-jet electropolisher from South Bay Technology Inc. (Model 550D) was used to prepare the TEM specimens. Normally, a mechanical grinding or thinning step is required prior to electrochemical polishing to obtain a large thin area in a perforated TEM specimen. However, mechanical thinning might produce a large volume of radioactive waste and possible spread of contamination. To contain the loose contamination, a procedure that relies solely on an electrochemical process was developed. By enlarging the hole and adding flow channels in the polyvinyl chloride cap of the pedestal of the electropolisher, TEM disks could be thinned uniformly from both sides to 100 μm before final perforation. An enlarged 3-mm jet nozzle was used in the thinning process. Once the desired thickness of TEM disk was achieved, the normal procedure to perforate a TEM disk was followed. The solution for SS specimens was 30ml $HClO_4$, 175ml Butyl Cellosolve and 295 ml Methanol. The optimized polishing condition for SS was -20°C and 70mA current with a diaphragm in place. For the nickel alloys, the solution was 10% HClO4 and 90% Methanol. The polishing condition for nickel alloys was -40°C and 110-125 mA current with a diaphragm. The height of jet nozzle was set at 3.5 mm from the assembly pedestal, and the flow rate was set at scale number 4 for all polishing.

To minimize radiation exposure during polishing, a Teflon diaphragm cap was fabricated to replace the original plastic diaphragm with an O-ring clamp used in the electropolisher. This modification facilitated the diaphragm alignment and reduced the exposure time considerably.

Occasionally, some samples needed to be re-perforated since the area around the original perforation was not sufficient for observation. The first step for re-perforation was to coat the central area on one side (relatively flat) of the specimen with lacquer while the rim was kept free of lacquer to make electrical contact with the specimen pedestal mount. After the lacquer was dry, an aluminum foil patch was placed over the original perforation and covered with lacquer. When the lacquer was dry, additional diluted lacquer was applied to the other side of the specimen, leaving a small uncoated area for re-perforation. The specimen was mounted with the uncoated area facing the jet nozzle. After the perforation, the lacquer was dissolved in acetone and the specimen was dried in air.

2.4.2 TEM Observation

For the irradiated materials, the void or bubble structure was examined by TEM under a bright-field kinematical imaging condition at high magnification. The through-focus technique which introduces a phase-contrast component (Fresnel fringes) due to defocus was used to image small voids. Because of the limitation of the microscope, voids smaller than 1 nm were not detectable.

The Frank loops in irradiated materials were examined by means of relrod dark field (DF) images. As one of the major microstructural defects in irradiated austenitic SSs, faulted dislocation loops with a Burgers vector a/3{111} lie on {111} planes. The relevant diffraction condition was obtained by tilting the sample close to the g = [311] two-beam condition near the zone axis [011], and the relrod DF images were formed by selecting the relrod streak with the objective aperture. One of the four variants of Frank loops was imaged by a relrod picture. Assuming an isotropic distribution, we determined the density of Frank loops from the measured density at this orientation by multiplying by four. The measurements were performed near the perforation edge in regions that were less than 80-nm thick, which minimized the overlap of defects and improved the accuracy.

3 Results

3.1 SSRT Test Results

3.1.1 SSRT Tests in Air

Baseline SSRT tests were conducted in air on two austenitic SSs (heats C21 of Type 316 SS and Heat 2333 of Type 304 SS obtained from ABB) in solution annealed (SA) and cold-worked (CW) conditions. Their compositions are given in Table 1. The purpose of the air tests was to establish a reference for the SSRT tests in water. All specimens were irradiated to ≈10 dpa for the tests in air. The test temperature and strain rate were ≈320°C and ≈7.4 x 10^{-7} s^{-1}, respectively. Figure 5 shows the engineering stress-strain curves for these tests.

Considerable irradiation hardening and irradiation embrittlement were observed in these tests. For the irradiated SA materials, the yield strengths (YS) were more than three times higher than those of the nonirradiated specimens. In addition, the elongation of irradiated materials was decreased. The increase in YS and the decrease in elongation were greater for irradiated specimens of the 35% CW materials. The differences in SSRT behavior between the Type 304 and 316 SSs were negligible for the same thermomechanical history, as shown in Fig. 5. Strain softening was observed for all irradiated materials. The CW specimens showed a much more rapid softening rate beyond the yield point.

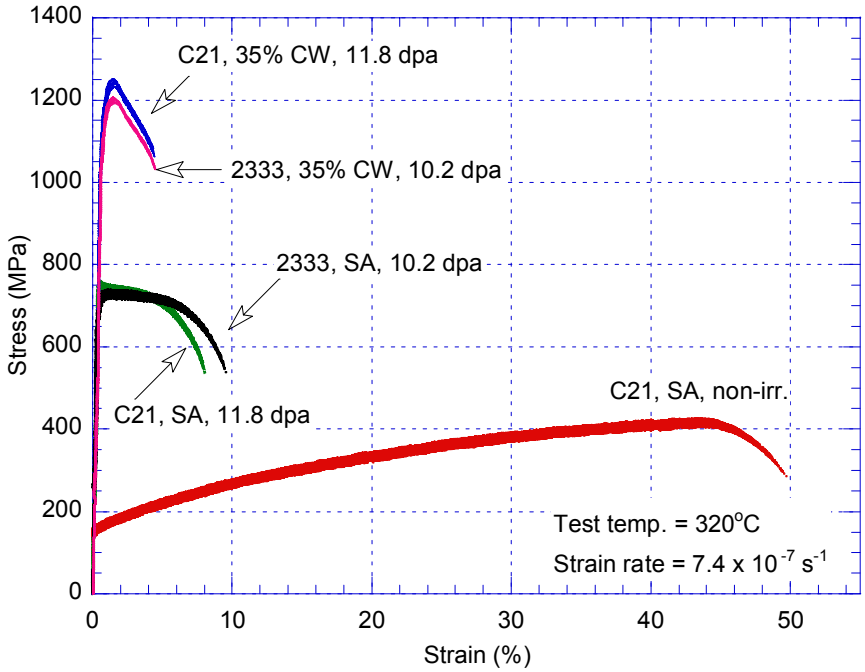

Figure 5. SSRT tests in air on BOR-60 specimens irradiated to approximate ≈10 dpa for Heat C21 (Type 316 SS) and Heat 2333 (Type 304 SS).

The scheme that was used to determine the tensile properties of the SSRT tests is described elsewhere.[19] If a well-defined yield point is present in a SSRT stress-strain curve, the YS is selected as the stress at the yield point; otherwise, the stress at 0.2% plastic strain is reported as the YS. The ultimate tensile strength (UTS) is defined as the maximum stress for the stress-strain curve. Thus, if during a SSRT test, strain softening occurs immediately after yield, the UTS would be the same as the YS. For a

strain-hardened material, the uniform elongation (UE) is the plastic strain at the UTS. For a strain-softened material (irradiated to a high dose), the plastic strain where the stress-strain curve starts to deviate from steady-state behavior is taken as the UE. The total elongation (TE) is defined as the plastic strain at fracture. The tensile properties of the SSRT tests in air are summarized in Table 4.

Table 4. Tensile properties of SSRT tests in air for selected BOR-60 specimens at 320°C.

Material	Heat ID.	Heat Treatment	Dose (dpa)	YS (MPa)	UTS (MPa)	UE (%)	TE (%)
Type 316 SS	C21	SA	-	162 (0.2%)	415	44	50
Type 316 SS	C21	SA	11.8	751	751	4.5	7.7
Type 316 SS	C21	CW	11.8	1237	1237	1.1	3.8
Type 304 SS from ABB	2333	SA	10.2	726	726	5.1	9.2
Type 304 SS from ABB	2333	CW	10.2	1092	1237	1.0	3.8

3.1.2 SSRT Tests in High-DO Water

The SSRT tests on selected BOR-60 specimens were performed in high-DO water at 289°C. The purpose of these tests was to compare the results with those obtained on identical materials that were irradiated in the Halden reactor. To single out the effect of irradiation conditions, we kept the SSRT test conditions for the BOR-60 specimens as close as possible to those for the Halden specimens.[19,20] The test environment for the BOR-60 specimens (DO, pH, conductivity, and temperature) was identical to that employed in the Halden SSRT tests, but the strain rate of the BOR-60 specimens (≈7.4×10^{-7} s^{-1}) was higher by a factor of two. Figure 6 shows the stress-strain curves of the SSRT tests in high-DO water at 289°C. The tensile properties obtained from these SSRT tests are summarized in Table 5.

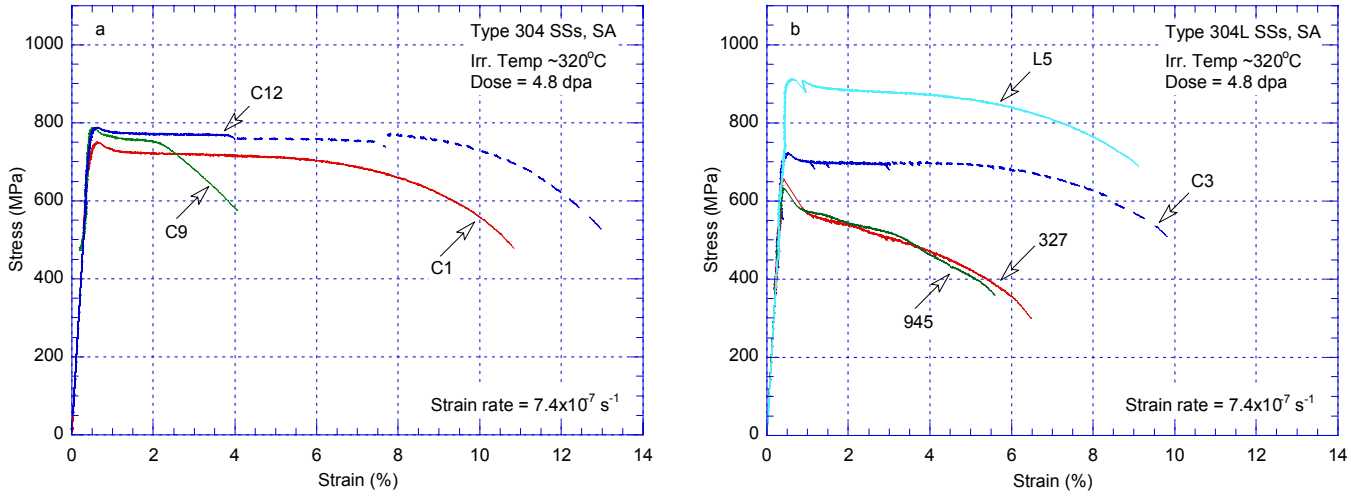

Figure 6. Stress vs. strain for SSRT tests in high-DO water at ≈289°C with selected BOR-60 specimens irradiated to ≈5 dpa: (a) Type 304 SSs and (b) Type 304L SSs. (The dashed lines represent the portions of the SSRT tests for the reloaded specimens.)

Table 5. Tensile properties of select BOR-60 specimens from SSRT tests in high-DO water at 289°C.

Material	Heat ID.	Heat Treatment	Dose (dpa)	YS (MPa)	UTS (MPa)	UE[a] (%)	TE[a] (%)
Type 304 SS with low S	C1	SA	4.8	750	750	5.6	10.5
Type 304 SS with low S	C12	SA	4.8	788	788	(8.2)	(12.6)
Type 304 SS with high S	C9	SA	4.8	788	788	1.6	3.7
Type 304L SS	C3	SA	4.8	723	723	(4.7)	(9.4)
HP 304L SS with low O	327	SA	4.8	659	659	3.8	6.4
HP 304L SS with high O	945	SA	4.8	632	632	2.9	5.4
304-like alloy	L5	SA	4.8	912	912	4.2	8.7

[a] Values in the parentheses are estimated.

3.2 Fractographic Results

3.2.1 Fracture Surface of Irradiated Specimen Tested in Air

The fracture surface of an irradiated specimen tested in air was examined by SEM. Figure 7 shows the cross section of the cold-worked Type 304 SS from ABB (Heat 2333 CW). No intergranular (IG) fracture is visible on the fracture surface. Ductile dimple fracture is dominant, and a small amount of mixed-mode fracture can also be seen. The non-ductility fracture areas are located at the center of the fracture surface, and are apparently associated with a complex local stress condition at the end of the SSRT test. Figure 8 shows the gauge surface of the same specimen, a little distance from the fracture surface. Plastic deformation is clearly visible on the gauge surface but is not extensive enough to cause many surface cracks.

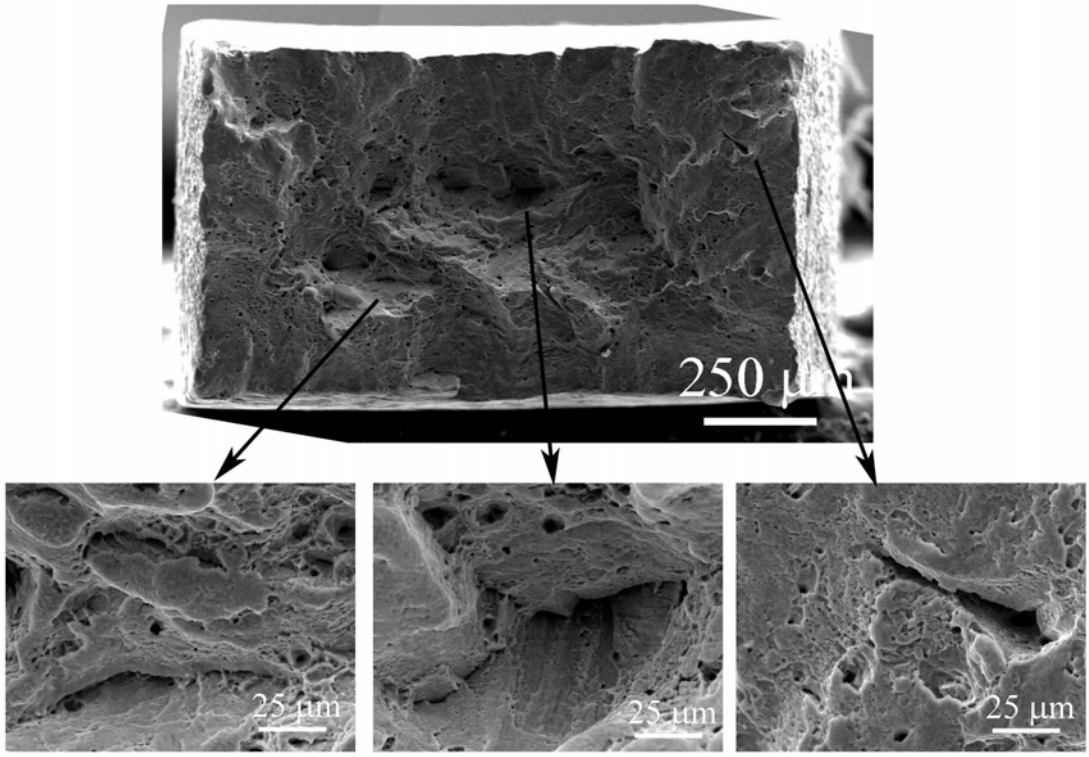

Figure 7. Fracture surface of an irradiated Type 304 SS CW from ABB (Heat 2333 CW) tested in air at 320°C.

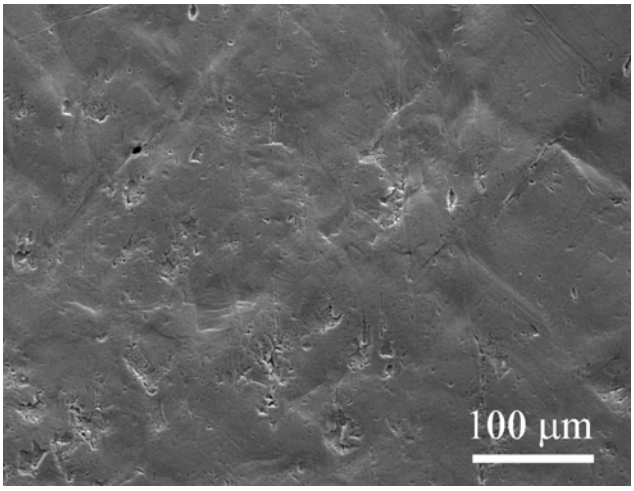

Figure 8.
Gauge surface of an irradiated Type 304 SS CW from ABB (heat 2333 CW) tested in air at 320°C

3.2.2 Fracture Surfaces of Irradiated Specimens Tested in High-DO Water

3.2.2.1 Type 304 SSs

Two low-S (from Heats C1 and C12) and one high-S (from Heat C9) Type 304 SSs were tested in high-DO water. Micrographs of the tested specimens appear in Figs. 9 to 14. Figures 9 and 11 show cross sections of the low-S SSs. Both specimens show a similar dimple fracture. No IG cracking was found. The gauge surfaces of both specimens were also similar (Figs. 10 and 12). Coarse slip lines appear on both specimens, and a few surface cracks can be seen in the heavily deformed region.

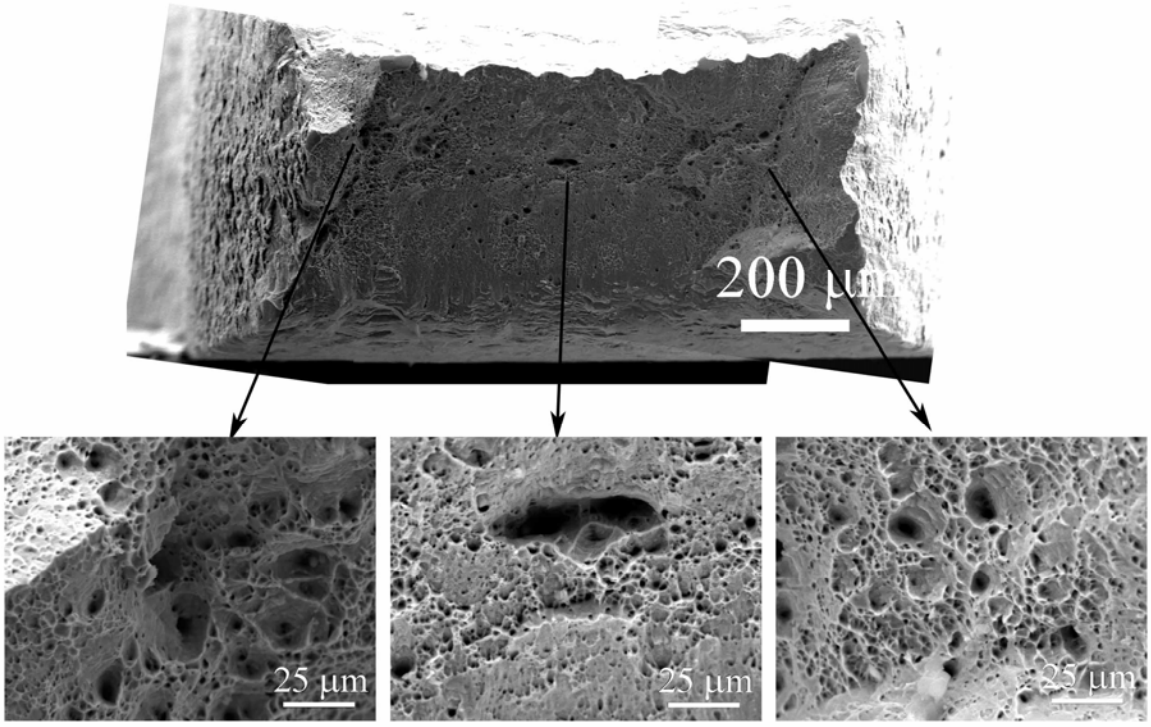

Figure 9. Fracture surface of a Type 304 SS with low-S content (Heat C1) tested in high-DO water at 289°C.

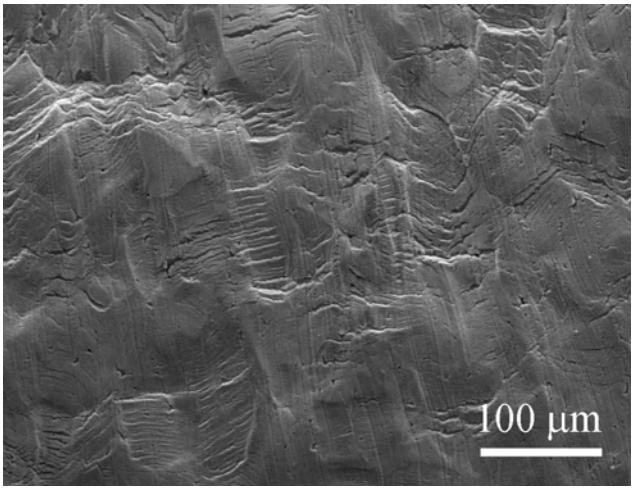

Figure 10.
Gauge surface of the Type 304 SS with low-S content (Heat C1) tested in high-DO water at 289°C.

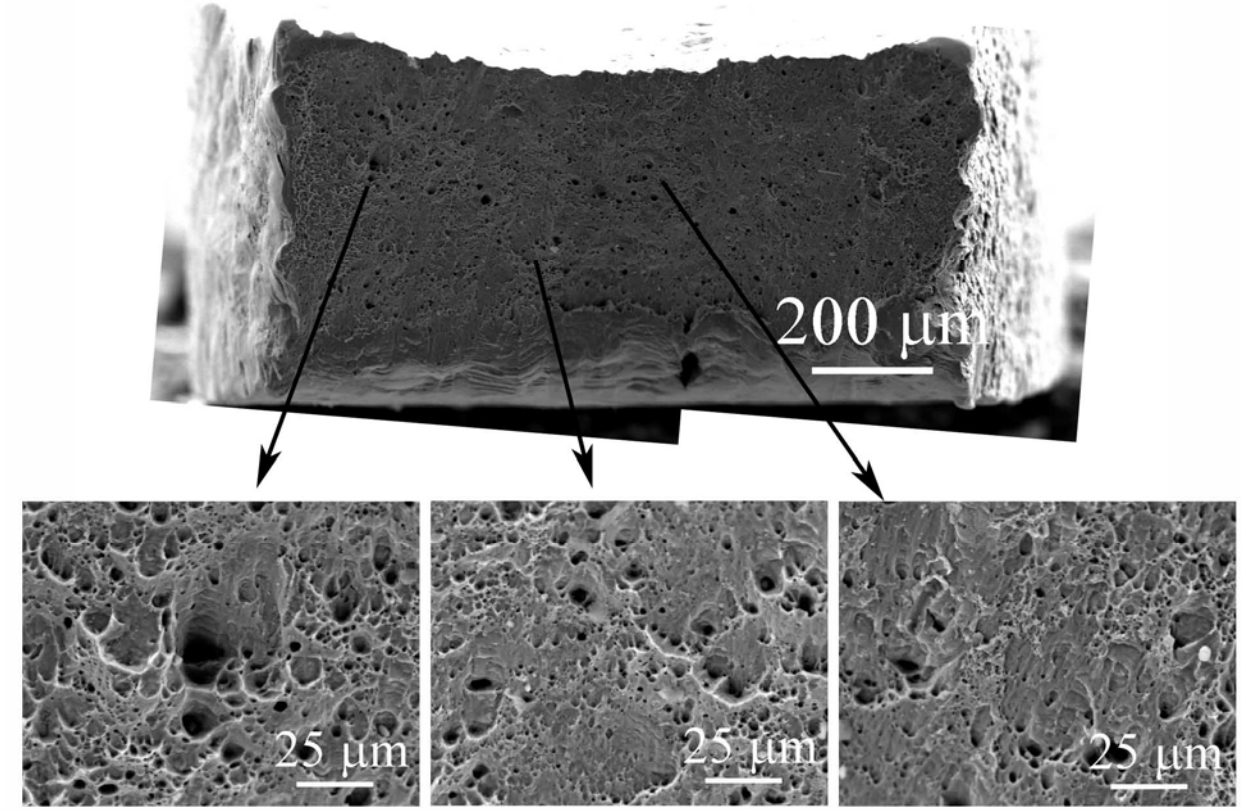

Figure 11. Fracture surface of another Type 304 SS with low-S content (Heat C12) tested in high-DO water at 289°C.

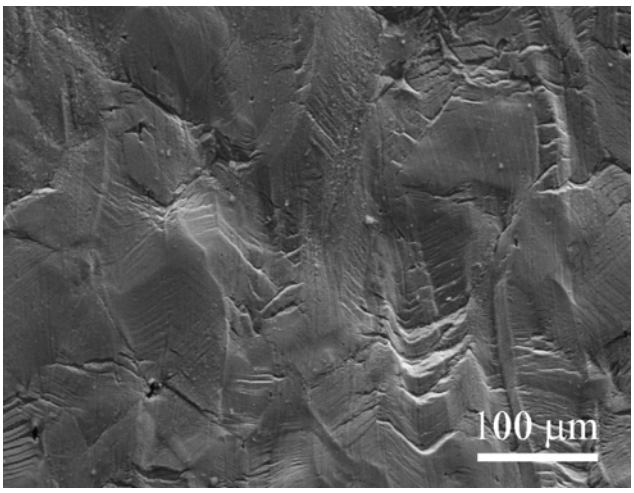

Figure 12.
Gauge surface of another Type 304 SS with low-S content (Heat C12) tested in high-DO water at 289°C.

A Type 304 SS with high-S content (Heat C9) was also tested in high-DO water. Figures 13 and 14 show the cross section and gauge surface of the specimen, respectively. More than half of the cross section (≈64%) exhibits IG cracking. Transgranular cleavage cracking and mixed-mode cracking can also be seen on the fracture surface. The IG cracking initiated at the specimen surface in contact with water and progressed towards the specimen interior. Several large longitudinal cracks are visible across the fracture surface. These longitudinal cracks are parallel to the loading direction and apparently are associated with the thermomechanical history of the material. The same longitudinal cracks also appear on the gauge surface, as shown in Fig. 14.

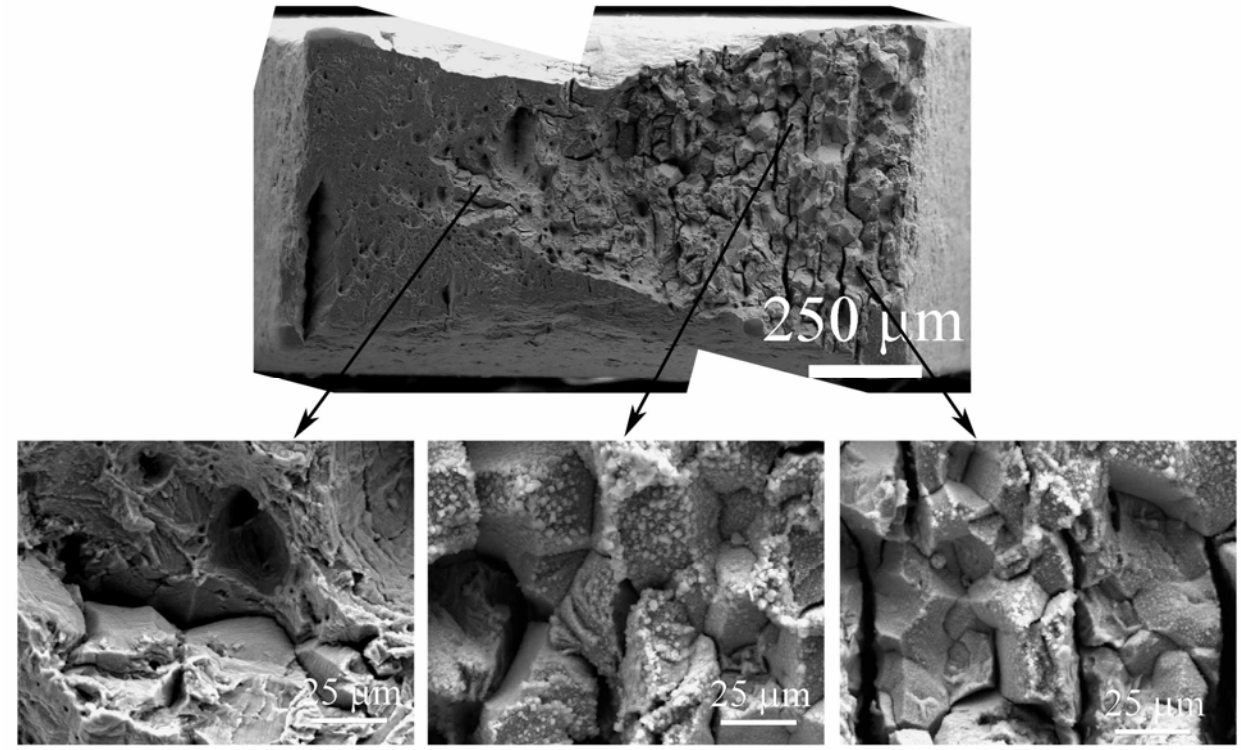

Figure 13. Fracture surface of a Type 304 SS with high-S content (Heat C9) tested in high-DO water at 289°C.

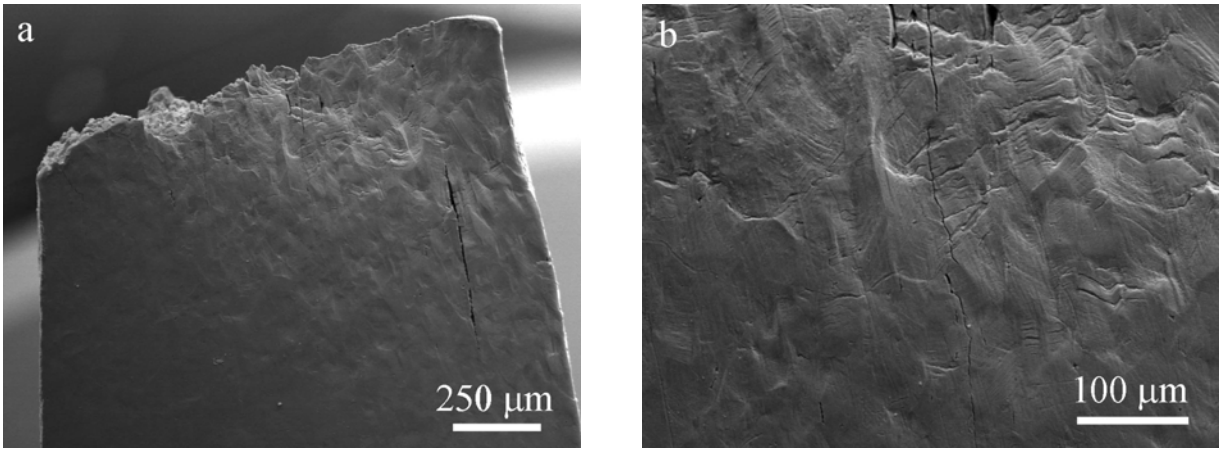

Figure 14. Gauge surface of the Type 304 SS with high-S content (Heat C9) tested in high-DO water at 289°C.

3.2.2.2 Type 304L SS

A Type 304L SS (Heat C3) was tested in high-DO water at 289°C. This specimen exhibited a complete dimple fracture. Two unexpected failures occurred prematurely in the specimen shoulders during this test. The specimen was re-loaded and tested until final failure. The complex fracture surface (Fig. 15) may be due to possible misalignment caused by specimen reloading. No IG fracture was detected in this specimen. The gauge surface of this specimen is relatively smooth, as shown in Fig. 16, and no surface cracking associated with plastic deformation was observed.

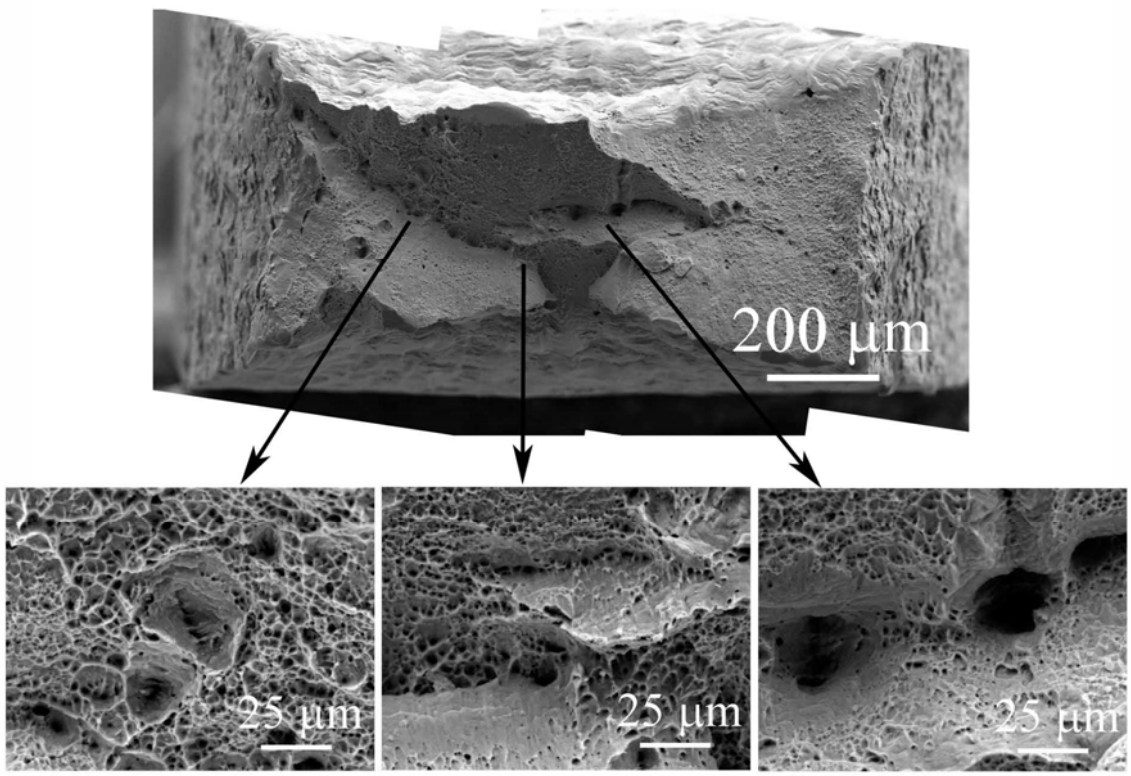

Figure 15. Fracture surface of a Type 304L SS (Heat C3) tested in high-DO water at 289°C.

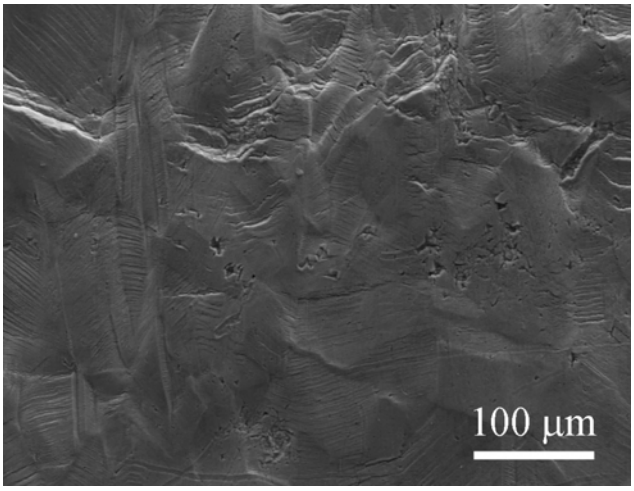

Figure 16.
Gauge surface of the Type 304L SS (Heat C3) tested in high-DO water at 289°C.

Figure 17 shows the fracture surface of a 304-like SS (Heat L5). This material contains a higher C content than that in Type 304L SS (Heat C3) but has significantly higher P and S contents (see Table 1). A fully ductile dimple fracture is also observed on the fracture surface. No IG cracking appears around the perimeter of the fracture surface. The uneven gauge surface shown in Fig. 18 indicates a considerable amount of plastic deformation near the fracture. Numerous surface cracks associated with heavy slip bands are also apparent on the gauge surface.

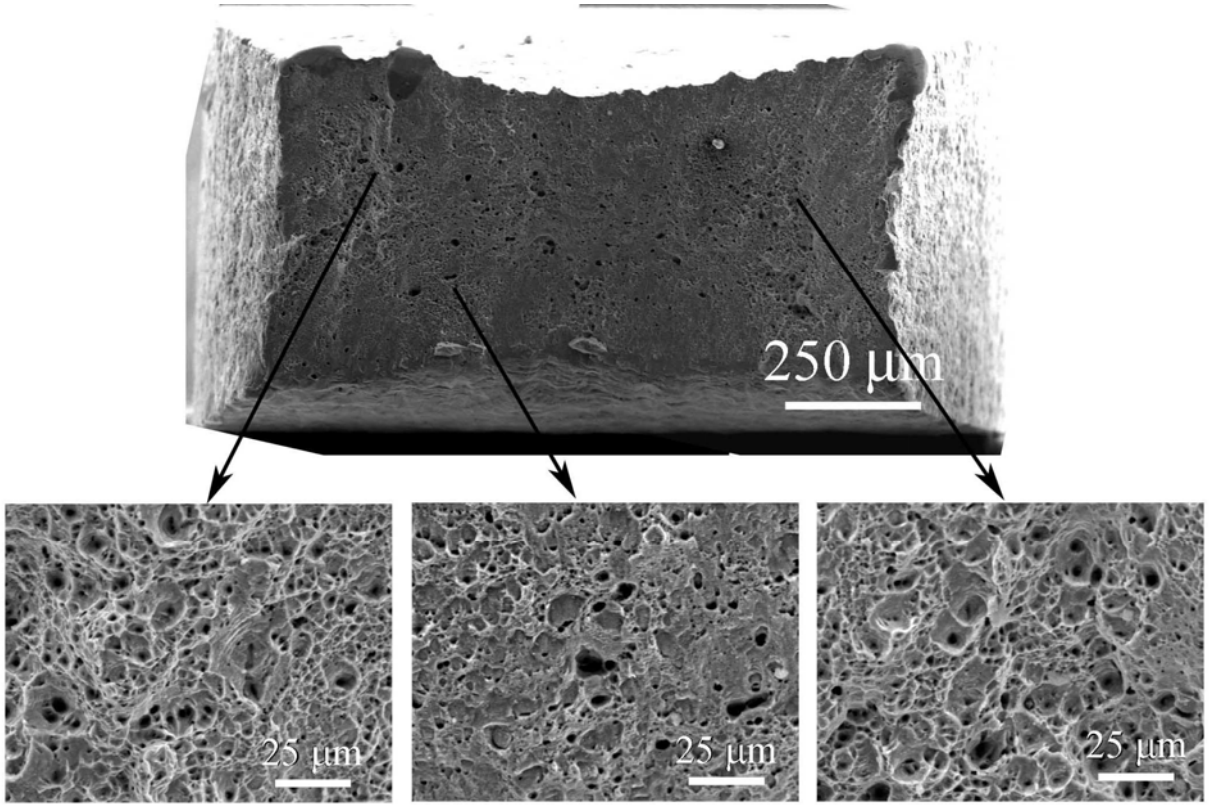

Figure 17. Fracture surface of a 304-like SS (Heat L5) tested in high-DO water at 289°C.

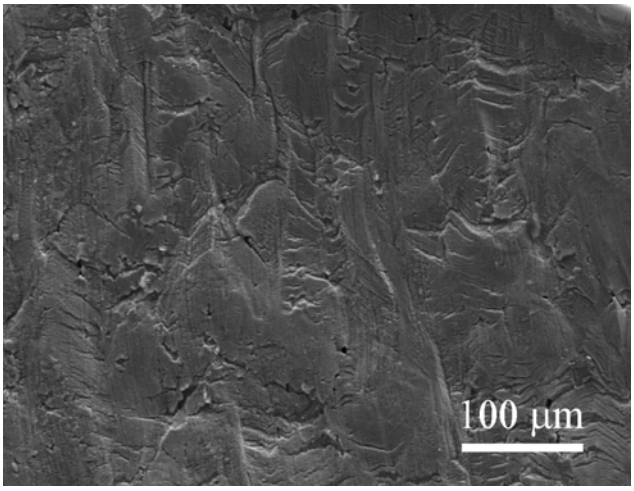

Figure 18.
Gauge surface of the 304-like SS (Heat L5) tested in high-DO water at 289°C.

3.2.2.3 High-Purity Type 304L SSs

Two high-purity (HP) Type 304L SSs, one with low-O (Heat 1327) and the other with high-O (Heat 945), were tested in high-DO water. Figures 19 and 20 show the fracture and gauge surfaces, respectively, of the low-O specimen. A significant amount of plastic flow occurred during the SSRT test, which resulted in a large reduction in area. The rupture morphology is essentially a ductile dimple fracture. No IG cracking can be seen. The gauge surface shows the typical coarse slip lines, but no surface crack could be found.

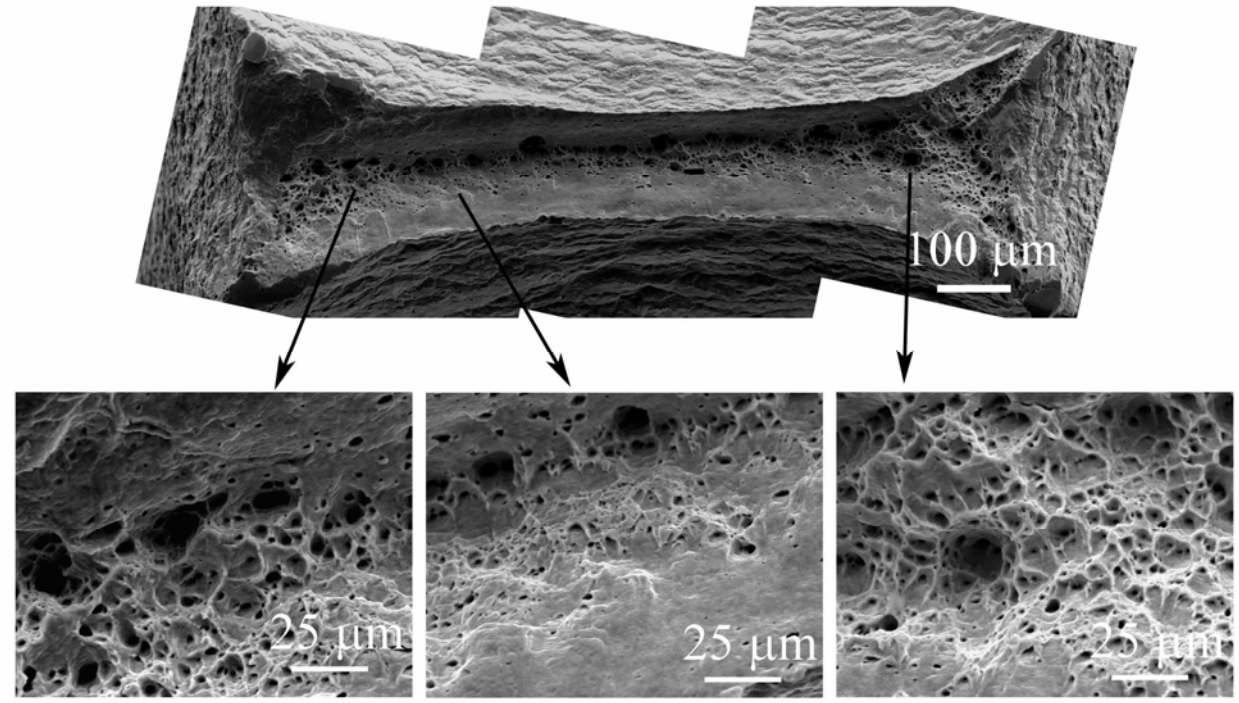

Figure 19. Fracture surface of a high-purity Type 304L SS with low-O content (Heat 1327) tested in high-DO water at 289°C.

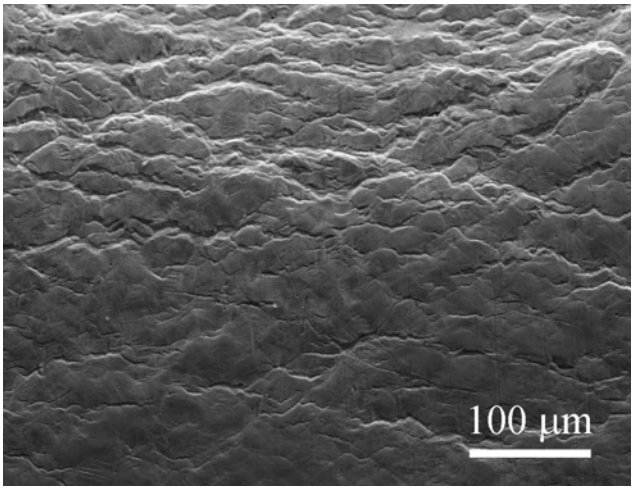

Figure 20.
Gauge surface of the high-purity Type 304L SS with low-O content (Heat 1327) tested in high-DO water at 289°C.

Another HP Type 304L SS has a much higher O content. Figures 21 and 22 show the cross section and gauge surface, respectively, of the high-O specimen. Three isolated IG cracking areas appear on the fracture surface. The total IG area fraction is ≈38%. Some transgranular cracking can also be seen between the IG cracking and dimple area. As shown in Fig. 22, the gauge surface adjacent to the area with IG cracking is much smoother than the area next to the dimple fracture. Corrosion pitting attack is also observed on the gauge surface.

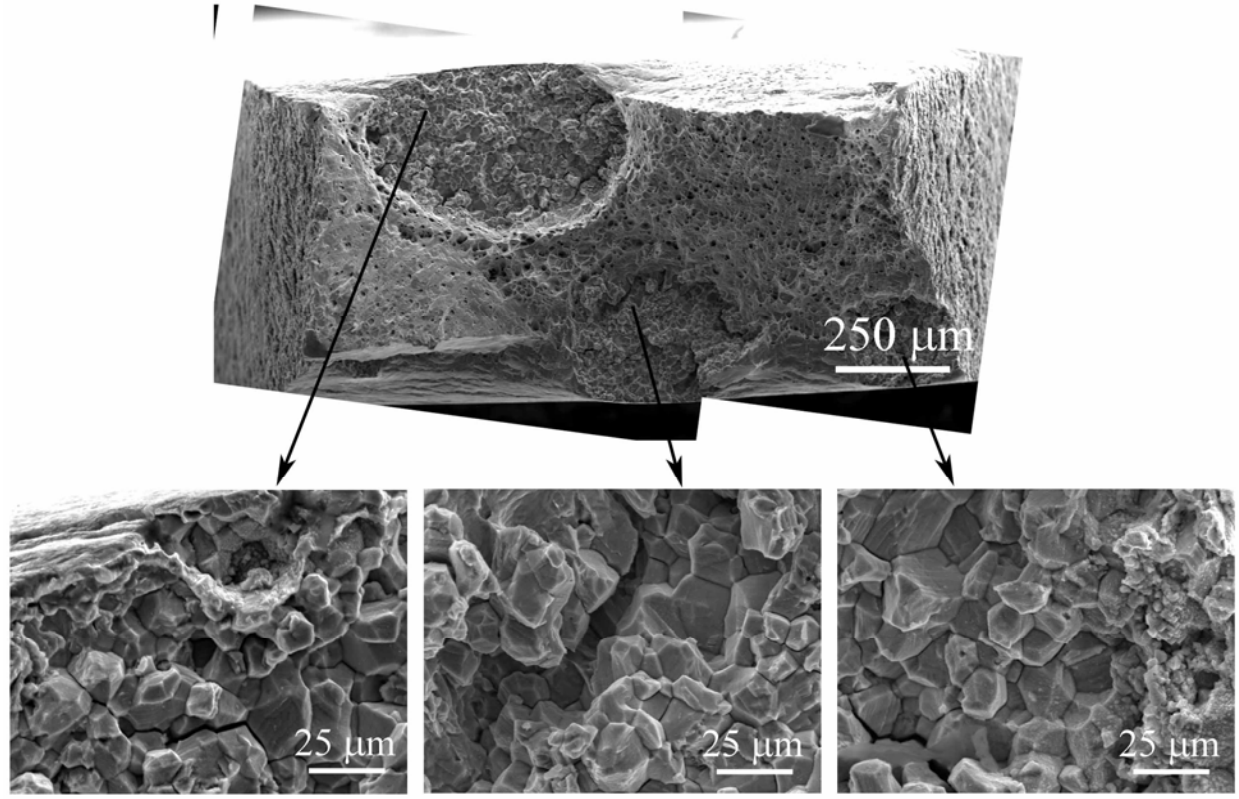

Figure 21. Fracture surface of a high-purity Type 304L SS with high-O content (Heat 945) tested in high-DO water at 289°C.

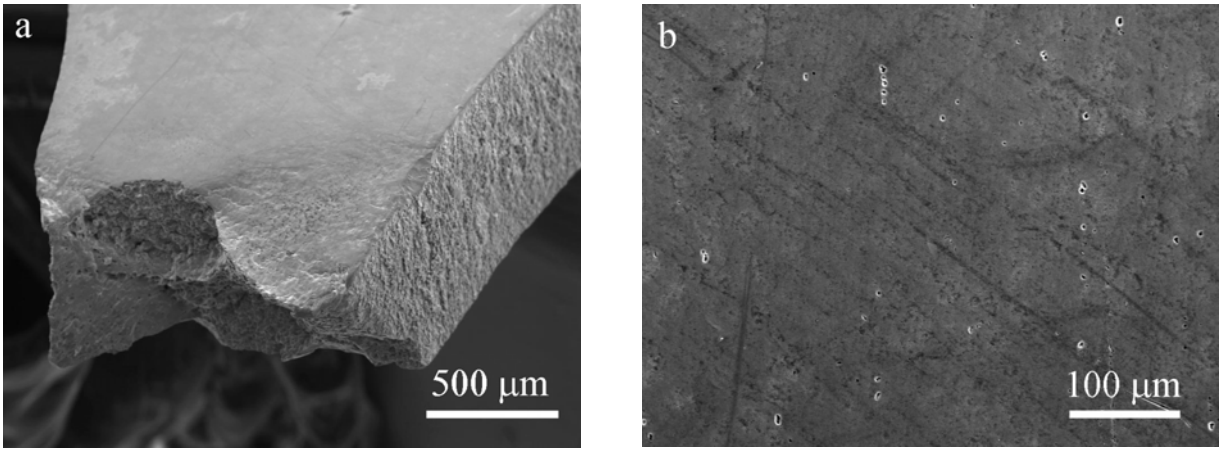

Figure 22. Gauge surface of the high-purity Type 304L SS with high-O content (Heat 945) tested in high-DO water at 289°C.

3.3 Irradiation Microstructure and Void Swelling

Ten 3-mm disks of wrought and cast austenitic SSs and nickel-base alloys, highlighted in Table 2, were selected for TEM examination. These specimens were irradiated in the BOR-60 reactor at ≈320 ºC to ≈25 dpa. The voids, dislocation loops, and radiation-induced precipitates were characterized.

3.3.1 Type 304 and 304L SSs

A TEM disk of SA Type 304 SS with low-S content (Heat C12) was polished for examination. No void was detected by the through-focus technique at high magnification. The irradiation microstructure shows a high density of dislocation loops in the bright field (BF) image in Fig. 23(a). Measuring the size and density of these faulted loops from a weak beam dark field (WBDF) image [e.g. Fig. 23(b)] is difficult because of the overlap between defects and their interacting strain fields. However, one-fourth of the total faulted dislocation loops is clearly visible in the dark field (DF) image shown in Fig. 23(c), which was obtained by the relrod technique. Figure 23(d) shows the size distribution of the Frank loops, with the major sizes ranging from 10 to 50 nm.

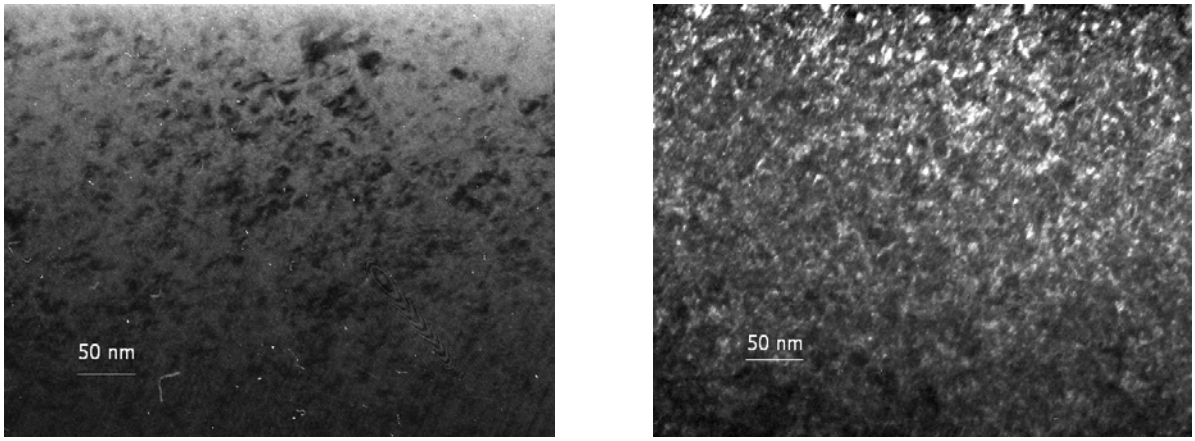

(a) (b)

Figure 23. Irradiated microstructure of Type 304 SS with low-S (Heat C12): (a) BF image; (b) WBDF image at g(3g), g=200; (c) relrod DF image of faulted loops; and (d) loop size distribution.

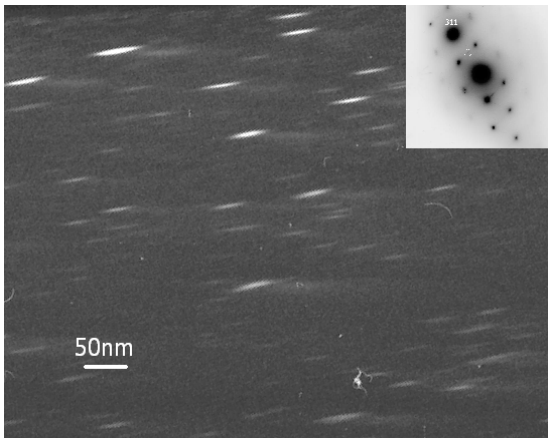

(c)

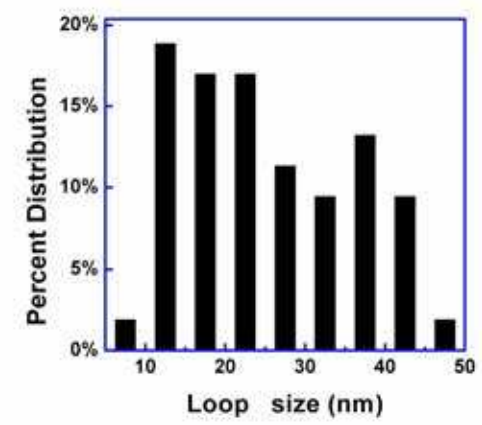

(d)

Figure 23. (Contd.)

Another SA Type 304 SS with high-S content (Heat C9) was examined. As shown in Fig. 24(a), the nonirradiated microstructure appears to be free of any dislocation network or black spots. Several dislocation loops can be observed in the BF image for the nonirradiated material, but the density is extremely low. No precipitate is seen in the nonirradiated material. Figure 24(b) shows the irradiated microstructure, which is also dominated by a high density of dislocation loops, and localized regions of high strain. The distribution of loop size is shown in Fig. 24(c), and the majority of the loops are between 2 and 15 nm. No voids were visible in this irradiated specimen.

A cold-worked (CW) Type 304 SS from ABB was also examined. As shown in Fig. 25, the significant features of a CW microstructure include twinning, dislocation cells, dislocation walls and microbands. The selected area diffraction (SAD) pattern shown in Fig. 25(d) demonstrates that the material was heavily textured, and the crystal was bent. The distortion of crystal lattices caused by CW led to the absence of Kikuchi patterns; this condition increases the difficulty in examining the irradiated microstructure.

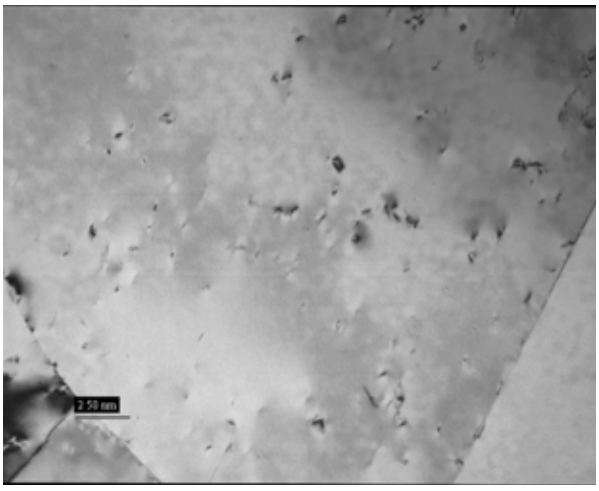

(a)

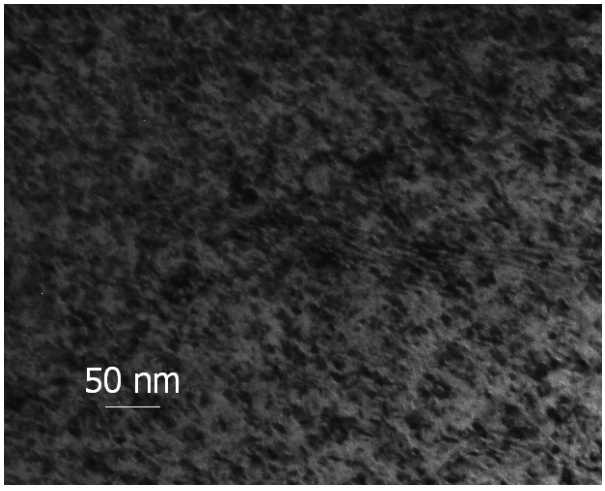

(b)

Figure 24. Microstructure of Type 304 SS with high-S content (Heat C9): (a) nonirradiated, BF image, (b) irradiated BF image, (c) irradiated relrod DF image, and (c) loop size distribution.

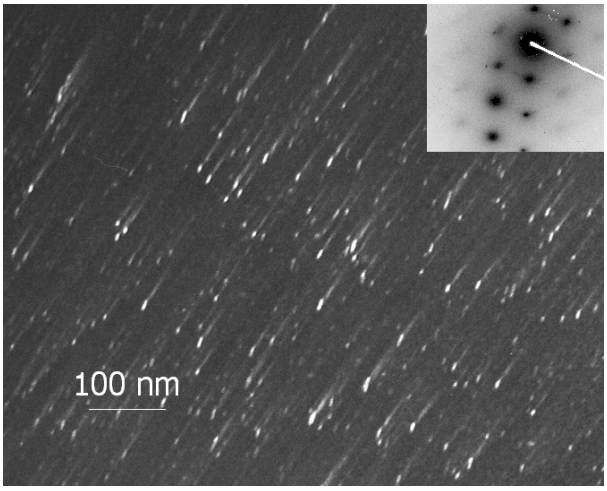

(c)

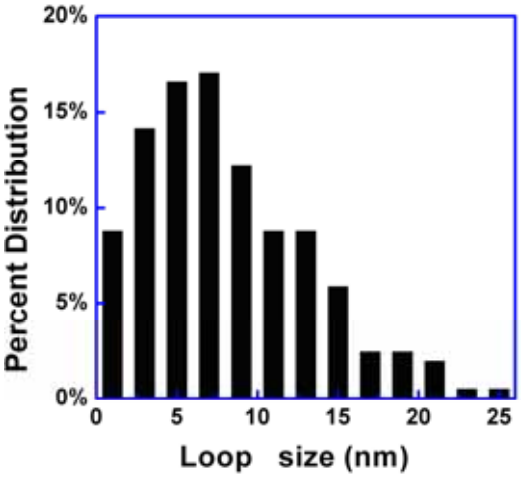

(d)

Figure 24. (Contd.)

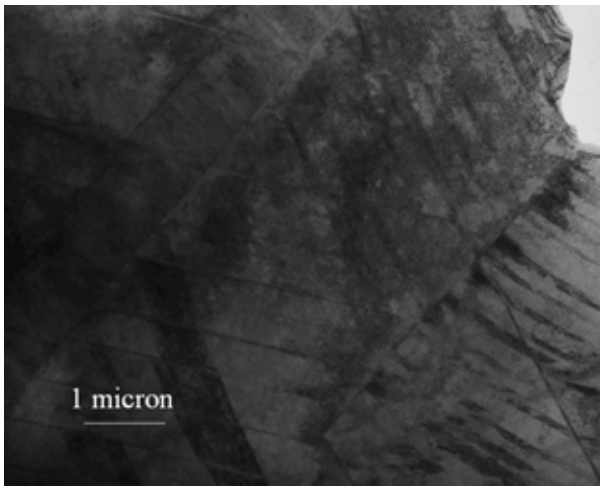

(a)

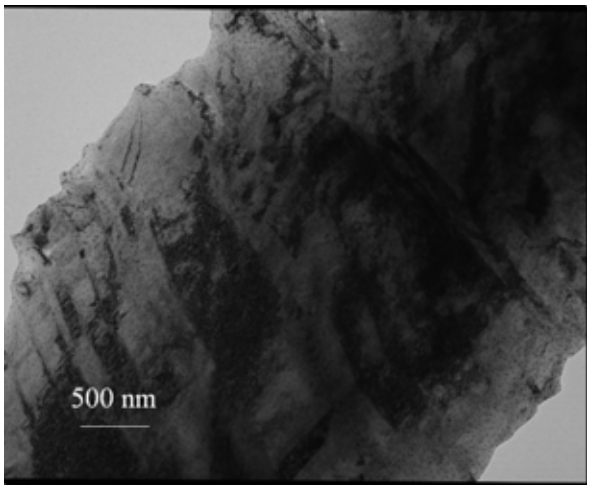

(b)

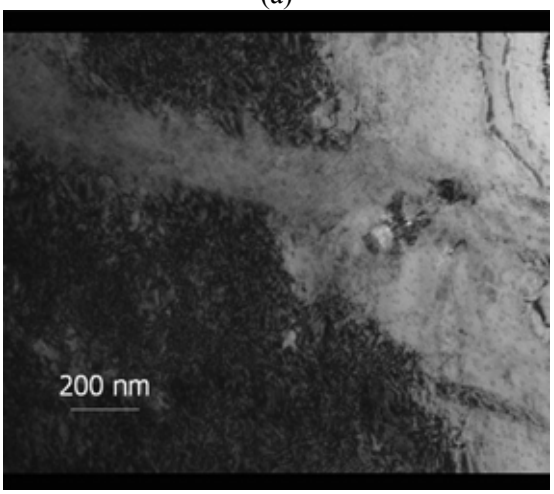

(c)

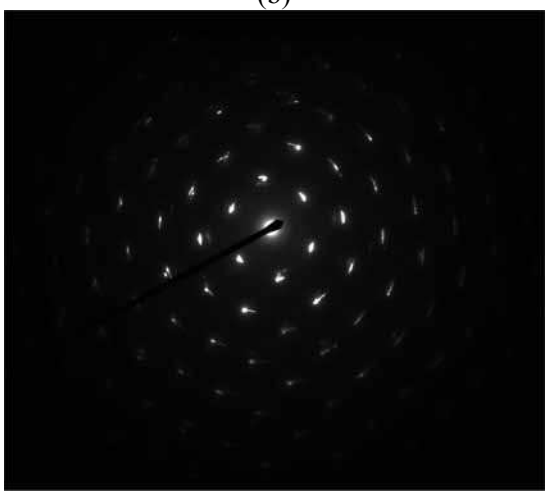

(d)

Figure 25. BF images (a-c) and SAD (d) for the nonirradiated CW Type 304 SS from ABB.

Figure 26 shows the irradiated microstructure of the irradiated CW Type 304 SS from ABB. Again, no voids were observed with the through-focus technique at high magnification. In the irradiated material, the density of dislocations in the dislocation cell was lowered, and some of the twinning introduced by CW became discontinuous. Large dislocation loops were observed, as shown in Fig. 26(b), and most of the dislocation loops were aligned along the CW walls; this finding suggests that the interstitials interacted with the CW dislocations and evolved into loops. However, because of the microstructural complexity caused by CW, the density of dislocation loops was not analyzed quantitatively.

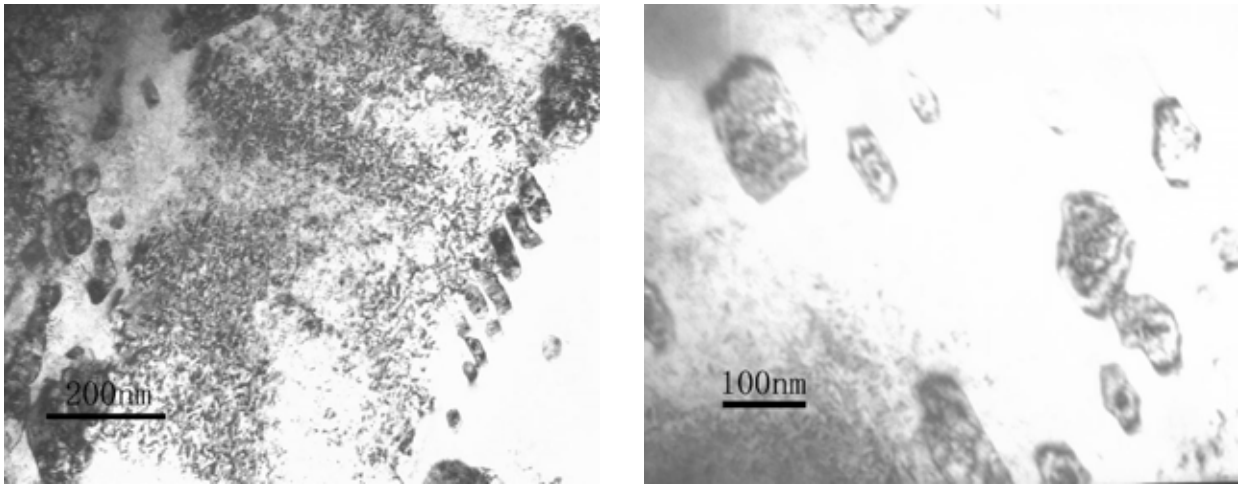

(a) (b)

Figure 26. BF images for the irradiated CW Type 304 SS from ABB (≈25 dpa).

The irradiated microstructure of an SA HP Type 304L SS with high-O content is shown in Fig. 27. The major defects are Frank loops and no voids are visible. As shown in Fig. 27(b), no denuded zone is noted around the grain boundary. The Frank loops are imaged in Fig. 27(c) by the relrod streak circled in the diffraction pattern. The size distribution of Frank loops is given in Fig. 27(d). The size of the Frank loops concentrates at <10 nm.

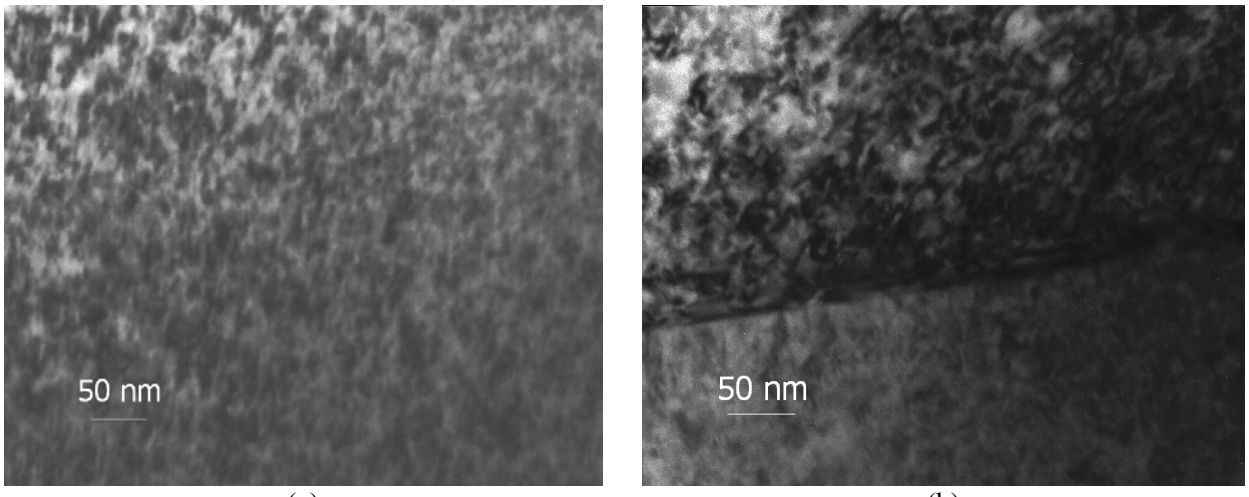

(a) (b)

Figure 27. TEM images of irradiated HP Type 304L SS with high O (Heat 945): (a) BF image, (b) grain boundary, (c) relrod image, and (d) loop size distribution.

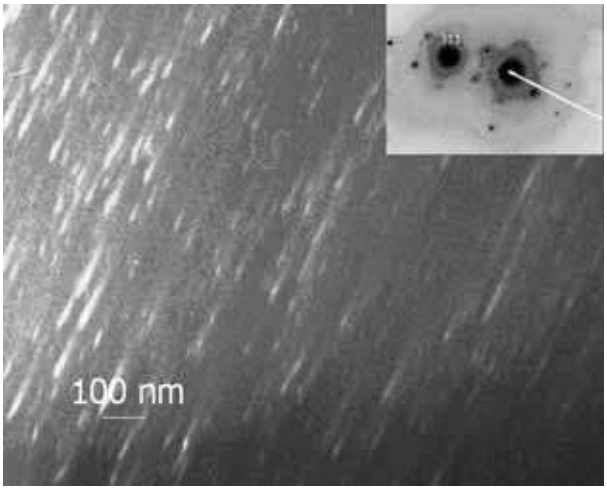

(c)

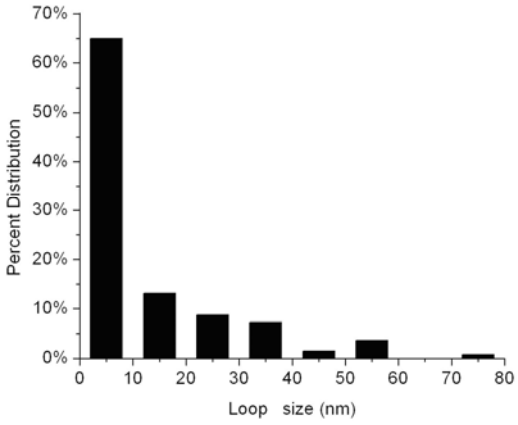

(d)

Figure 27. (contd.)

3.3.2 Type 316 LN SS

The nonirradiated microstructure of the Type 316 LN SS is illustrated in Fig. 28. The heavily textured microstructure indicates that the material had not annealed to completely remove the preexisting microstructure. The starting condition for the irradiated specimen may contain a relatively high density of dislocations.

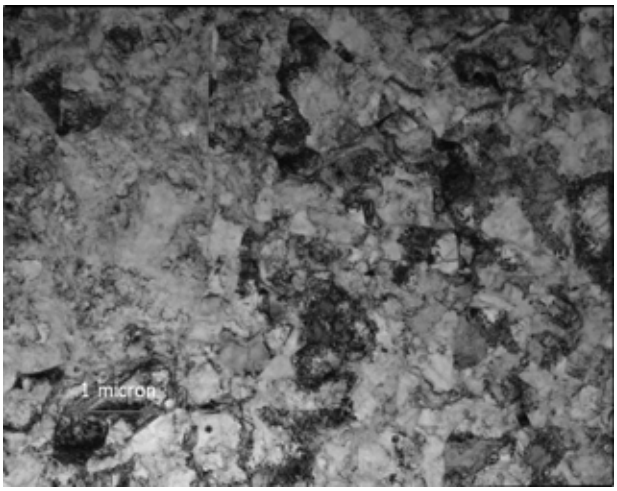

(a)

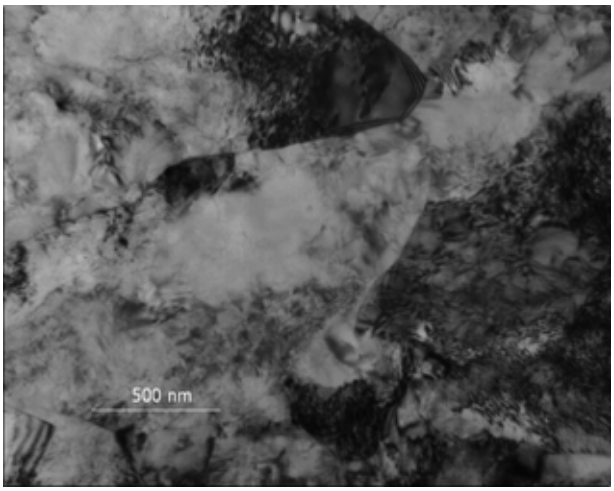

(b)

Figure 28. TEM images of the nonirradiated Type 316 LN SS (Heat 623).

Figure 29 shows the irradiated microstructure of the Type 316 LN SS. Compared with the nonirradiated material, Fig. 29(a) clearly shows the black spot damage. Precipitates were observed at the sub-grain-boundary as shown in Fig. 29(b). The size of precipitates is less than 20 nm, and the chemical composition could not be obtained due to the limitation of the microscope. Figure 29(c) shows the relrod DF image of the Frank loops in this material. The most popular size of Frank loops in this specimen is about 3 nm, as shown in Fig. 29(d).

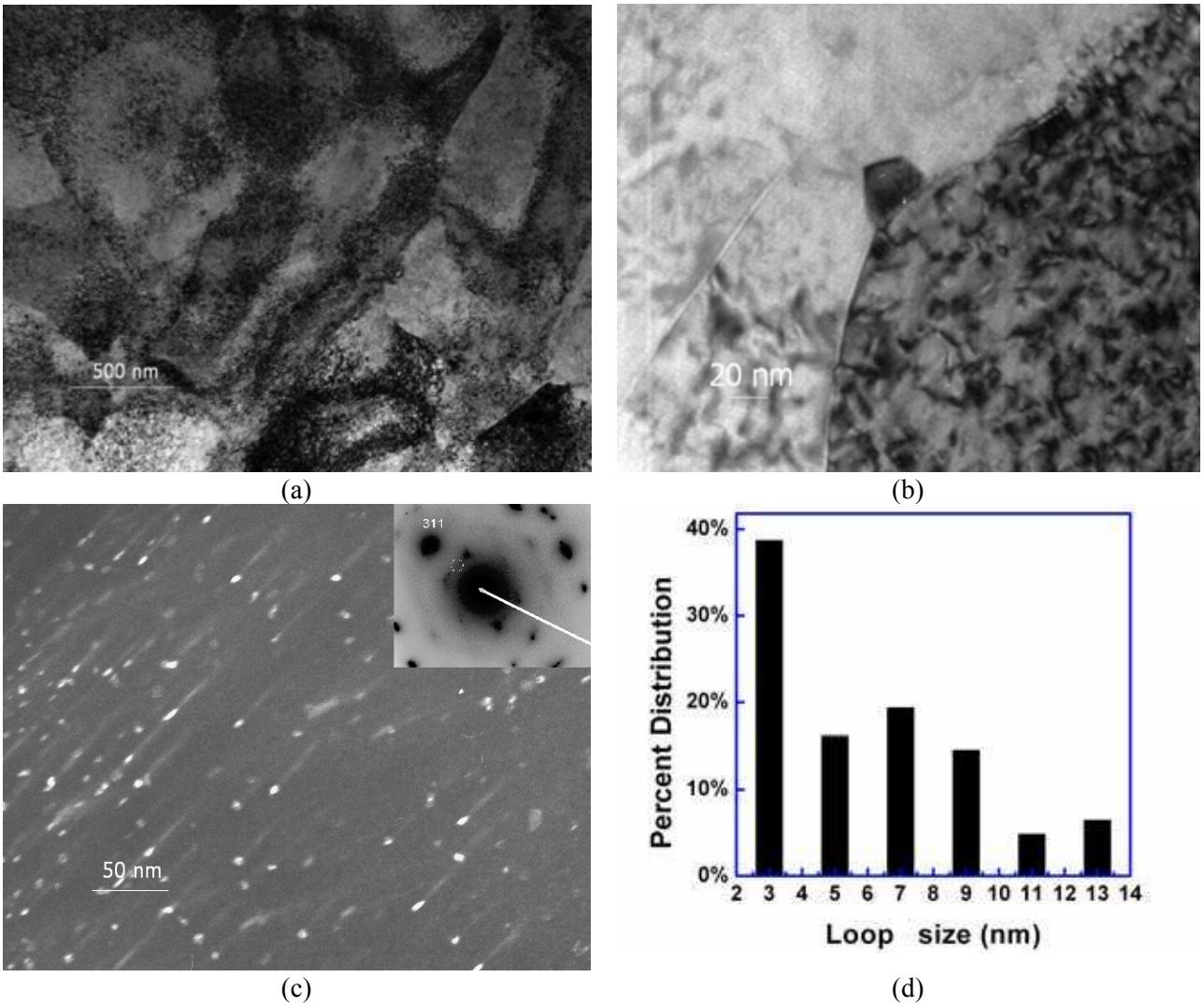

Figure 29. TEM images of the irradiated Type 316 LN SS (Heat 623): (a) BF image, (b) grain boundary, (c) relrod DF image, and (d) loop size distribution.

3.3.3 Ferrite/Austenite Duplex Cast SSs

The microstructure of two CF-8 cast SSs (Heats 59 and 68 with 13.5% and 23.4% ferrite, respectively) was characterized. The nonirradiated microstructure of Heat 68 is shown in Fig. 30. The nonirradiated material is nearly free of dislocation defects, and the ferritic phase is clearly shown as an island band among austenite phases. The irradiated microstructure of Heat 68 is dominated by a high density of dislocations, while no voids appear in either phase, as shown in Fig. 31. Compared with the austenitic phase, the ferrite has a lower density of dislocation loops. The dislocation loop size distribution in austenite is illustrated in Fig. 31(d), which shows that most of the loops are smaller than 30 nm.

Figure 30.
BF image of nonirradiated CF-8 cast SS (Heat 68).

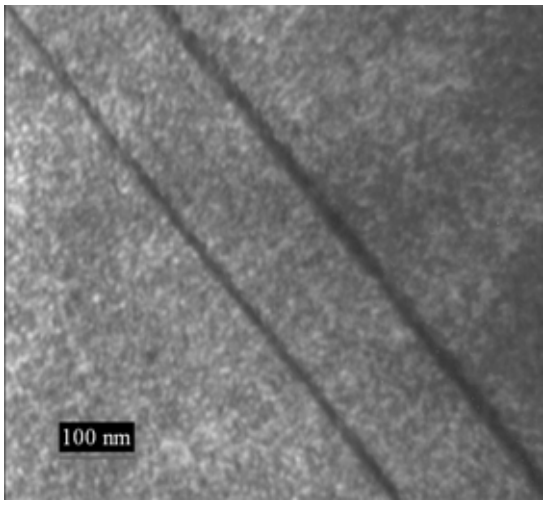

(a)

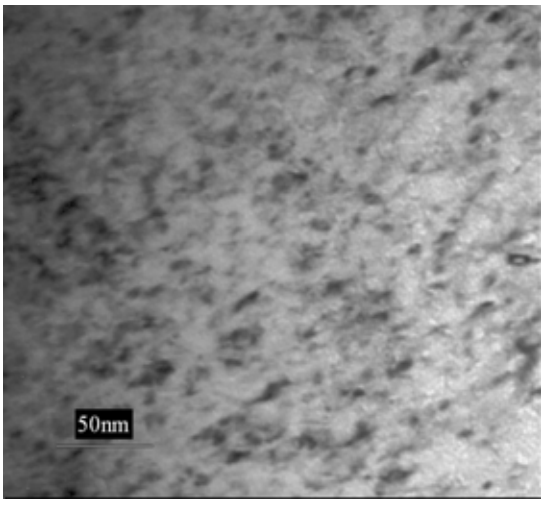

(b)

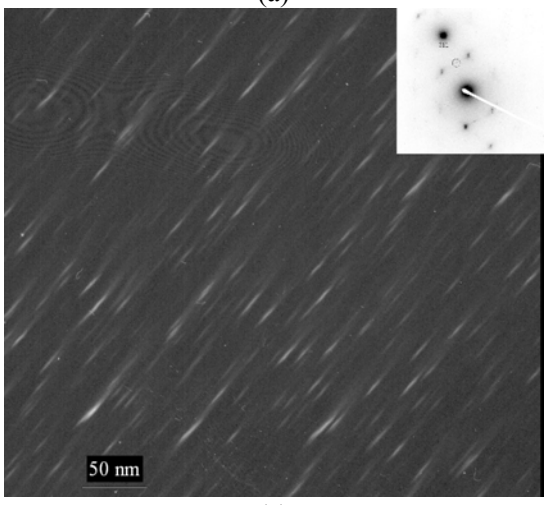

(c)

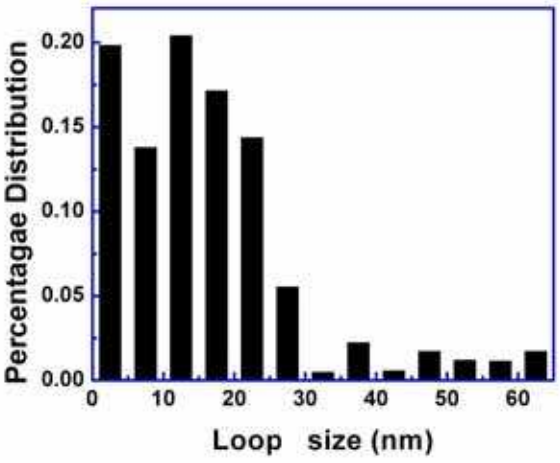

(d)

Figure 31. TEM images of CF-8 cast SS with 23.4% ferrite (Heat 68): (a) BF image of austenitic phase, (b) BF image of ferritic phase, (c) relrod image of dislocation loops in austenite, and (d) diffraction condition for the relrod image

The irradiated microstructure of the CF-8 cast SS (Heat 59) is shown in Fig. 32. Similar to Heat 68, the ferrite phase has a lower density of dislocation loops than the austenite phase, as shown in Fig. 32(a). No detectable precipitates were found at the austenitic/ferrite grain boundary, and no voids appeared in either phase. Compared with Heat 68, the dislocation loop size in this material is smaller, with most of the loops being less than 15 nm, as shown in Fig. 32(c).

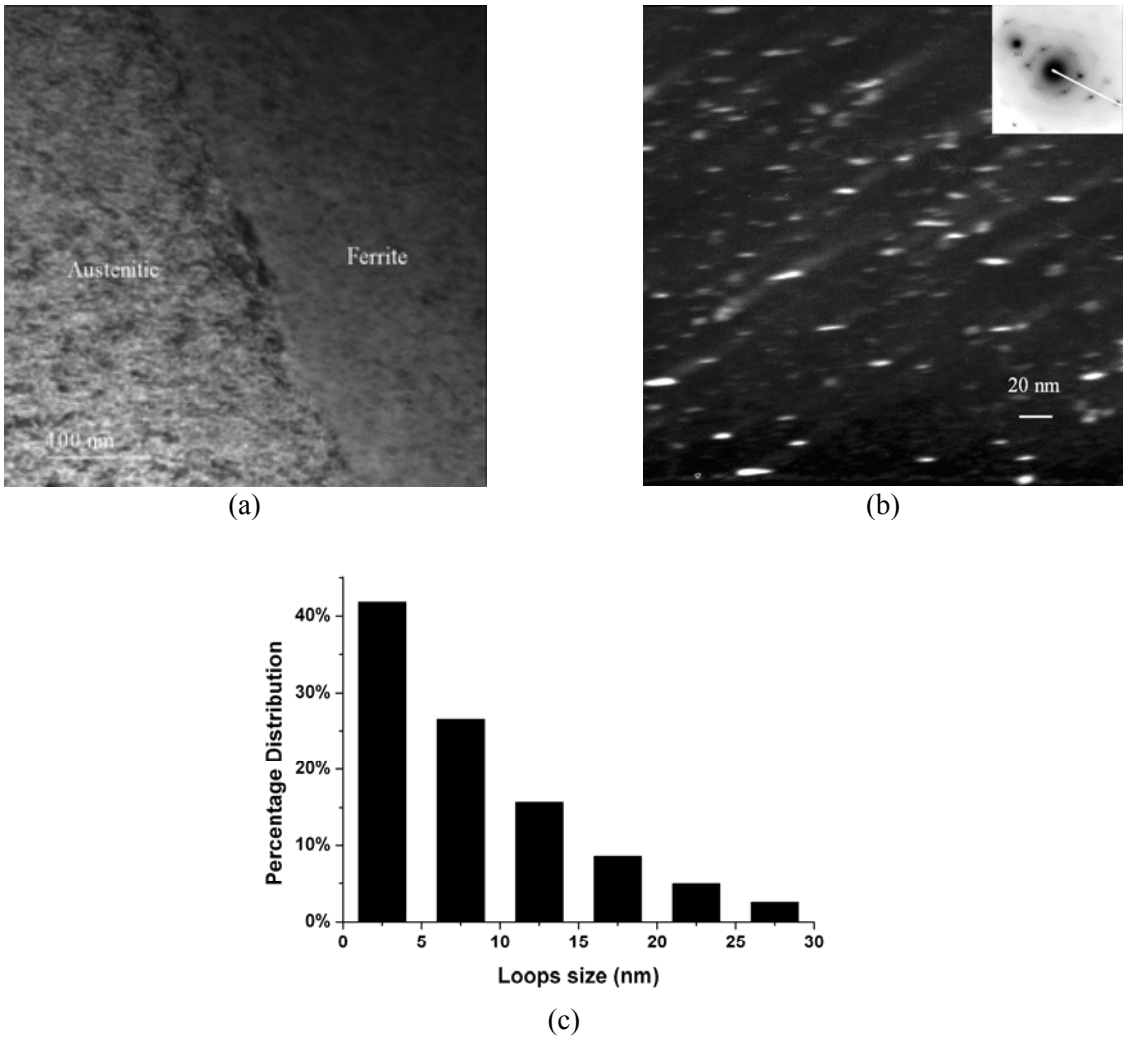

(a) (b)

(c)

Figure 32. Irradiated microstructure of another CF-8 cast SS with 13.4% ferrite (Heat 59): (a) austenite/ferrite grain boundary, (b) relrod DF image in austenite, and (c) loop size distribution in austenite.

The irradiated microstructure of the low-C CF-3 cast SS with 13.5% ferrite (Heat 52) is also dominated by a high density of dislocations (Fig. 33). The ferritic phases appear as island bands among austenite phases. No voids appeared in either the austenite or ferrite. Compared with the austenite, the ferrite has a lower density of dislocation loops, as shown in Fig. 33(b). No precipitates or defect-denuded zones were identified near the grain boundaries of the austenite and ferrite. The Frank loops were visualized by a relrod DF image and relatively strong relrod streaks were observed in the diffraction pattern, as shown in Fig. 33(c). The loop size distribution in austenite is plotted in Fig. 33(d), with most of the loops being smaller than 10 nm.

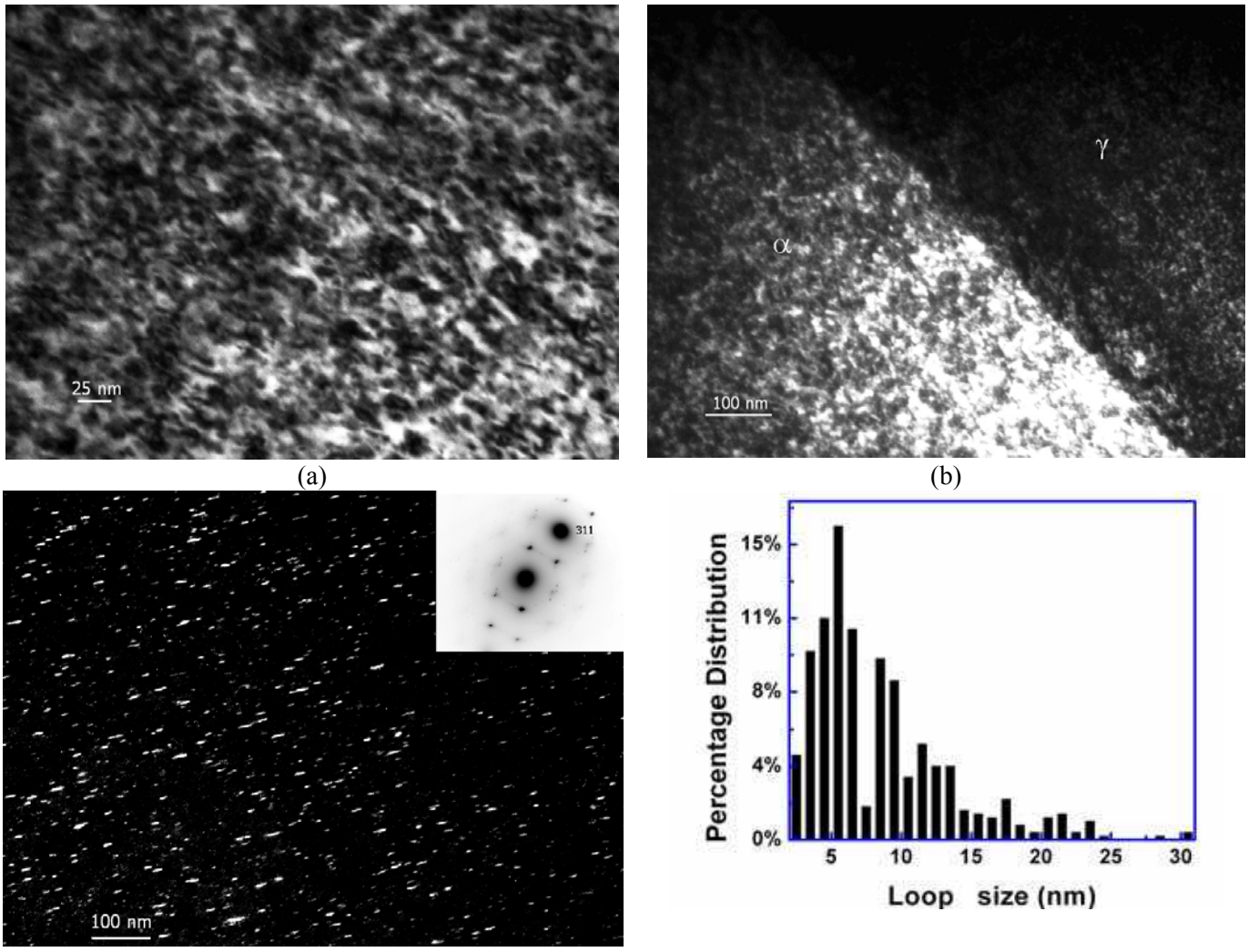

Figure 33. Irradiated microstructure of CF-3 cast SS with 13.5% ferrite (Heat 52): (a) BF image of austenitic phase, (b) BF image of grain boundary of austenite and ferrite, (c) relrod DF image in austenite, and (d) loop size distribution in the austenite.

3.3.4 Nickel Alloys

The microstructure of Alloy 690 with and without GBE treatment (Heats 690BASE and GBE690) is shown in Figs. 34 and 35. Prior to the irradiation, both alloys contained a high density of twin bands. Both materials also had many precipitates mainly distributed at the grain boundaries. The precipitates were identified as $M_{23}C_6$ chromium-rich carbides that have a face-centered cubic structure with a measured lattice constant of 1.062 nm (Fig. 36). The size and distribution of the intergranular carbides varied at different grain boundaries. Additionally, the nonirradiated microstructure was free from dislocation defects in both materials.

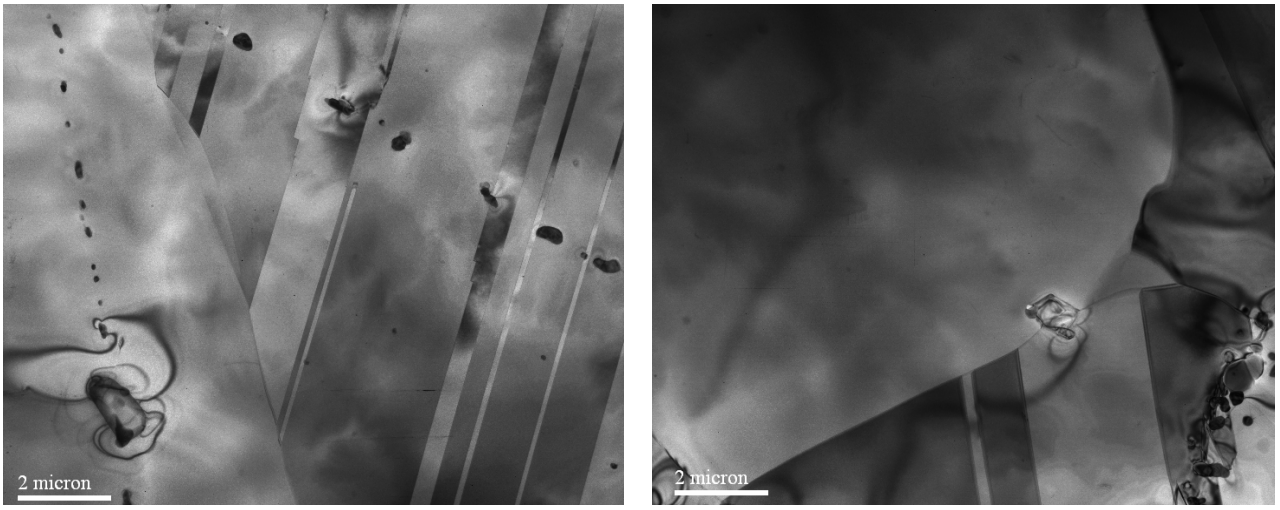

(a) (b)

Figure 34. Nonirradiated microstructure of Alloy 690 without GBE treatment (Heat 690BASE): (a) twin bands, and (b) precipitates at grain boundary.

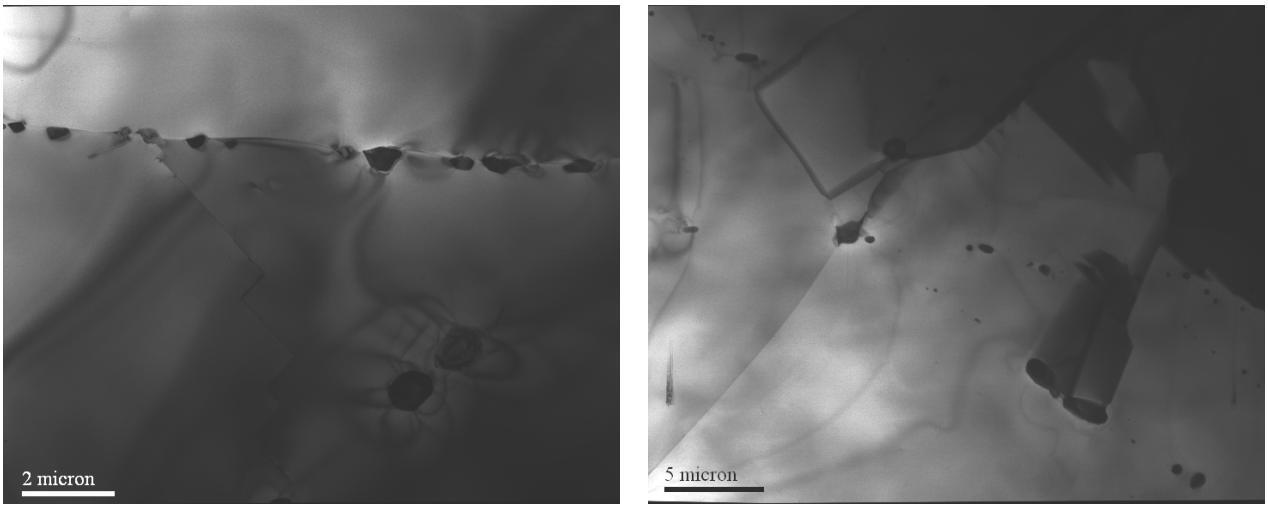

(a) (b)

Figure 35. Nonirradiated microstructure of Alloy 690 with GBE treatment (Heat GBE690).

The irradiated microstructure of Alloy 690 is shown in Fig. 37. Voids are clearly present in the irradiated Alloy 690 as demonstrated in Fig. 37(a) and (b), but the density is extremely low. The voids are scattered throughout the material and are mainly associated with grain boundaries or paired with precipitates. The size of the voids varies from ~25 to ~65 nm. The precipitates in the irradiated material are similar to those observed in the nonirradiated material. The faulted Frank loops are distributed uniformly throughout the irradiated material, with a mean size around 30 nm, as shown in Fig. 37(e).

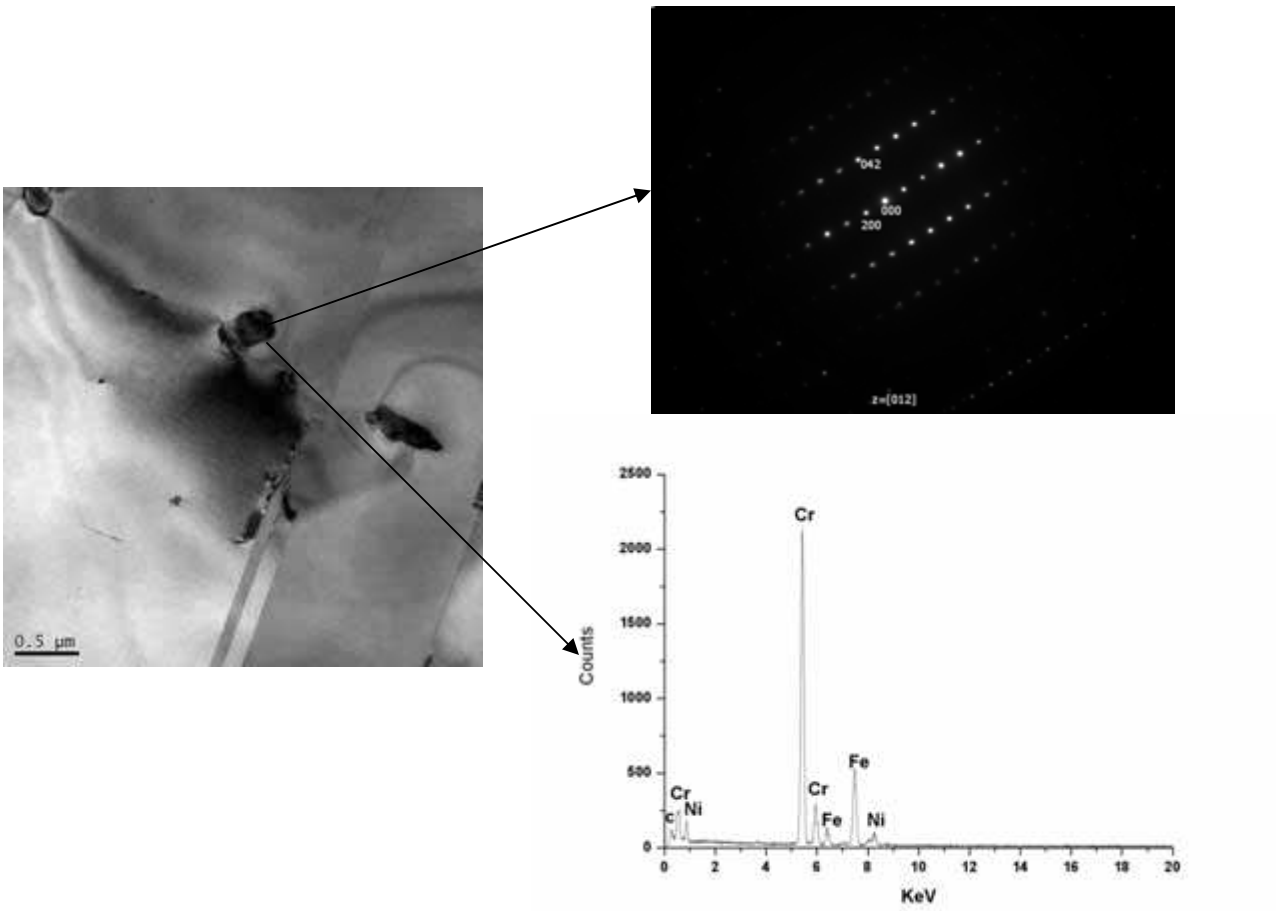

Figure 36. Diffraction pattern and EDS spectrum of $M_{23}C_6$ precipitate in the nonirradiated Alloy 690.

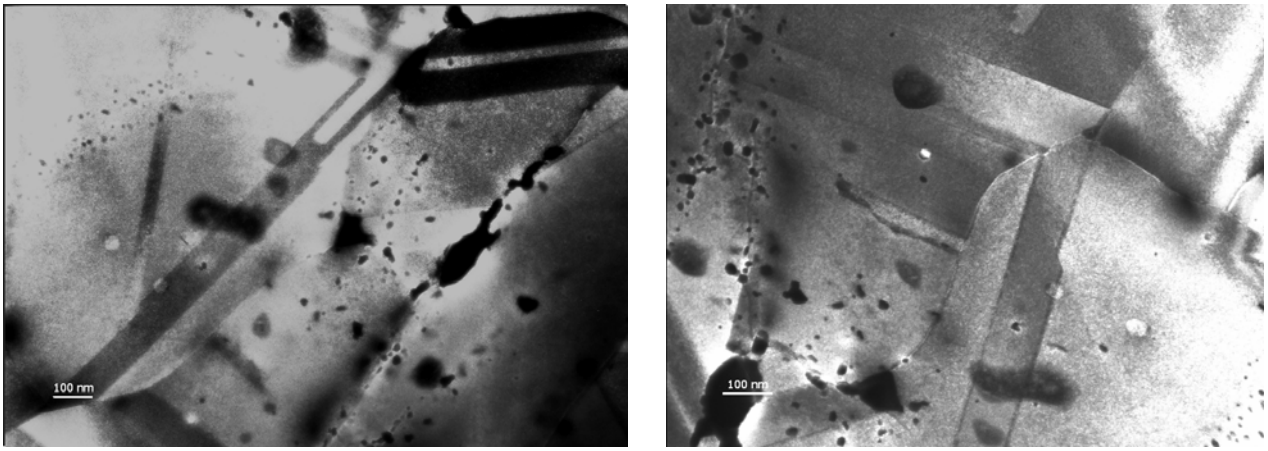

(a) (b)

Figure 37. Irradiated microstructure of Alloy 690 (Heat 690BASE): (a and b) voids in BF image at g = 200, (c) BF image of dislocation structures, (d) relrod DF image of dislocation loops, and (e) loop size distribution.

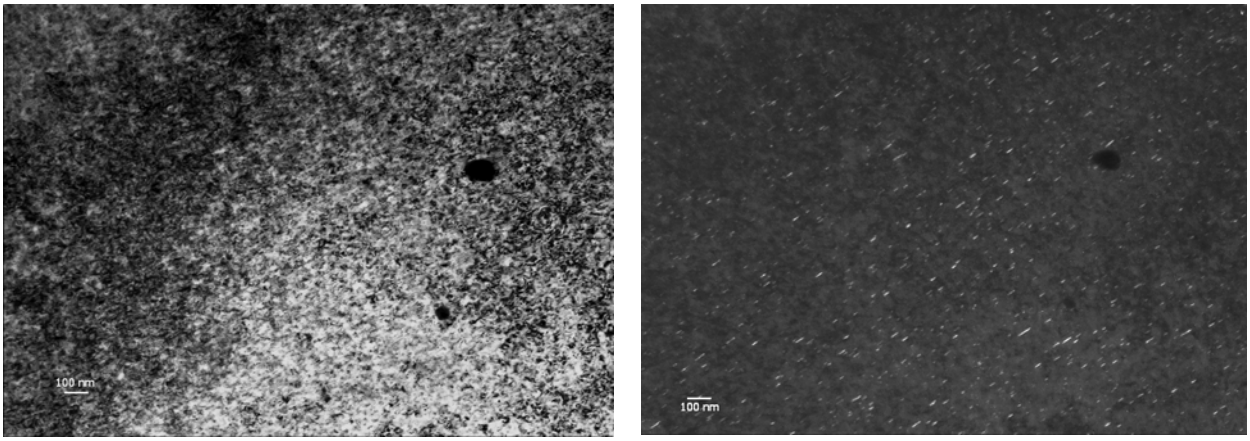

(c) (d)

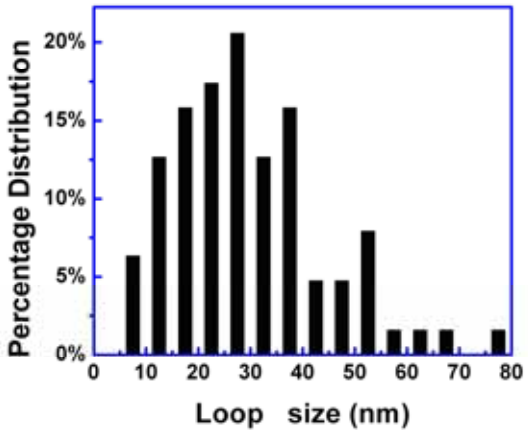

(e)

Figure 37. (Contd.)

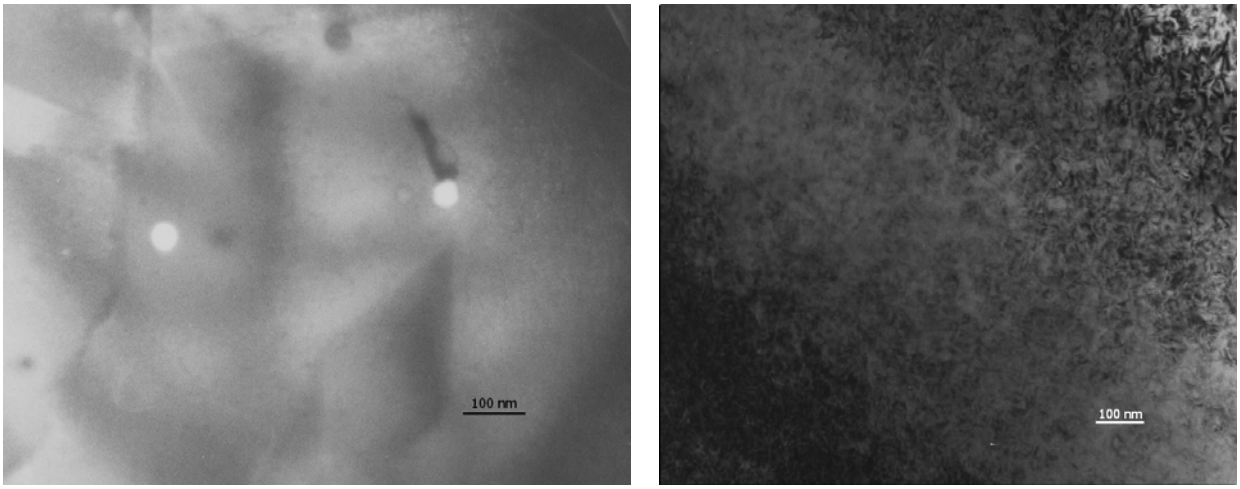

(a) (b)

Figure 38. Irradiated microstructure of GBE Alloy 690: (a) voids in BF image at g = 200, (b) BF image of dislocation structures, (c) relrod DF image of dislocation loops, and (d) loop size distribution.

The irradiated microstructure of GBE Alloy 690 is shown in Fig. 38. A few voids were also observed in GBE Alloy 690 after irradiation. Compared with the irradiated base alloy, the voids in the GBE-treated alloy have a lower density and larger size, as displayed in Fig. 38(a). The dislocation loop

structures are shown in Fig. 38(b) and (c). The loop mean size in the GBE Alloy 690 is smaller than that in the base alloy.

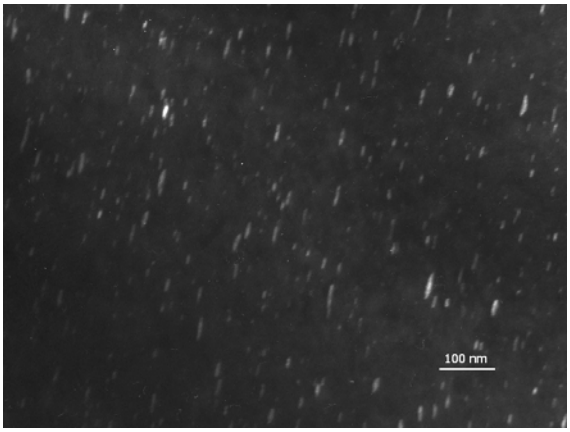

(c)

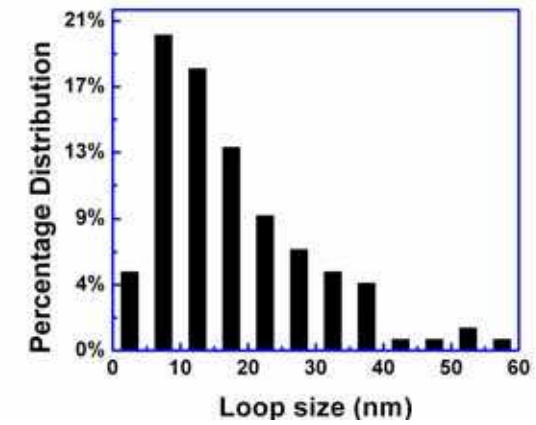

(d)

Figure 38. (Contd.)

4 Discussion

4.1 Comparison of SSRT Tests on BOR-60 and Halden Specimens

4.1.1 Irradiation Effects on the SSRT Properties

The SSRT test conditions for both the Halden and BOR-60 specimens were identical with the exception of the strain rate. The strain rate was ≈3.31 x 10^{-7} s^{-1} for the Halden specimens and ≈7.4 x 10^{-7} s^{-1} for the BOR-60 specimens. However, a factor of about two increase in the SSRT strain rate is not enough to cause a change in either strength or ductility.

Figure 39 shows the YS of some SA austenitic SSs irradiated at 90 to 427°C and tested in various environments between room temperature and 427°C. In spite of the limited data in the high dose region, a general trend of irradiation hardening is evident by the shaded area in the figure. Apparently, the YS of SA SSs starts to saturate between 3 and 5 dpa. This behavior is consisted with literature data, which indicate irradiation hardening starts to saturate at around 3-10 dpa for austenitic SSs.[24,25] Studies on irradiation microstructure show that, although the saturation dose for various irradiation defects varies from 0.1 dpa to 30 or 40 dpa, the total dislocation density in austenitic SSs reaches a common saturation value at around ≈5 dpa.[26,27,28] The dose range for the BOR-60 and Halden specimens in this study is close to, or slightly below, the saturation dose for austenitic SSs.

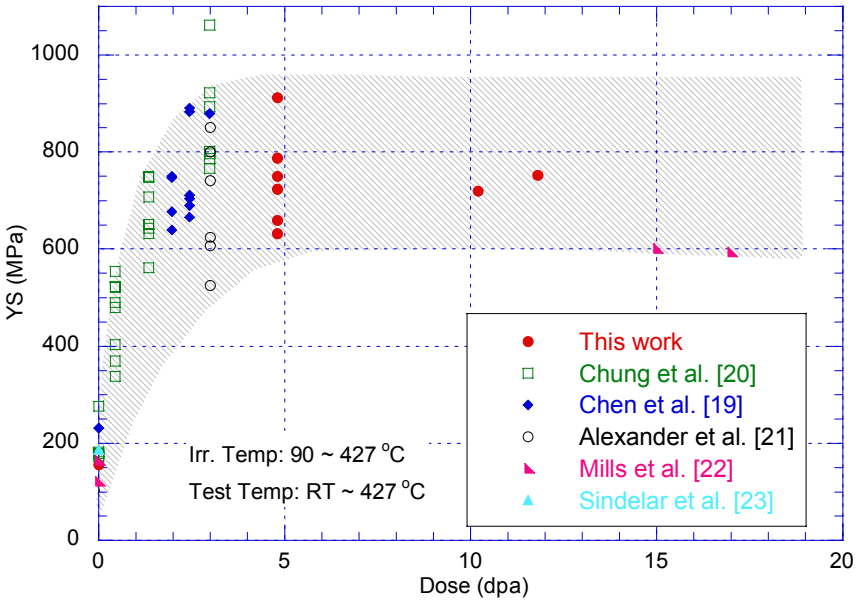

Figure 39.
Yield strength of SA austenitic SSs irradiated at 90 to 427°C and tested in various environments between room temperature and 427°C.[19-23]

The SSRT results between the BOR-60 and Halden specimens are compared in Table 6. The Halden specimen C9 failed immediately after yield, so no information on its UTS or UE is available. For the BOR-60 specimens, all three Type 304 SSs have a similar YS, which implies they have a similar microstructure after irradiation. However, the UE of the high-S alloy is much smaller than that of the low-S alloys. This difference may be associated with the cracking behavior of irradiated materials in high-DO water and is consistent with the findings from the Halden irradiation study. For Type 304L SSs, the YSs of the tested specimens vary from 632 to 912 MPa, while their UEs are comparable. The SSRT tests on HP Type 304L SSs with low- and high-O content are very similar. Both stress-strain curves show

dramatic load drops beyond yield. Similar SSRT behavior was observed for the same materials in the Halden study.[19]

Table 6. Comparison of SSRT results from BOR-60 and Halden specimens.

Material	Heat ID	YS (MPa)		UTS (MPa)		UE (%)		IG (%)	
		BOR-60	Halden	BOR-60	Halden	BOR-60[a]	Halden	BOR-60	Halden
304 SA, low S, SA	C1	750	802	750	833	5.6	3.38	-	-
304 SA, high S, SA	C9	788	-	788	-	1.6	-	64	94
304 SA, low S	C12	788	922	788	996	(12.7)	1.28	-	2
304L SA	C3	723	796	723	826	(9.5)	5.05	-	26
304-like alloy	L5	912	953	912	985	4.2	0.59	-	4
HP304L, SA, low O	327	659	703	659	703	3.8	1.51	-	1.4
HP304L, SA, high O	945	632	666	632	666	2.9	1.22	38	22

[a] Data in the parentheses are estimated values due to sample reloading in the SSRT tests.

Despite the similar SSRT test conditions, the tensile properties resulting from the two irradiations are slightly different. Both the YS and UTS are higher for the Halden specimens (Fig. 40), while the UE is larger for the BOR-60 specimens (Fig. 41). Although the irradiation dose for the BOR-60 specimens (≈5 dpa) is somewhat higher than that of the Halden specimens (≈3 dpa), the YS for the BOR-60 specimens is nearly 50 MPa lower than that of the Halden specimens. A similar difference is also found in the UTS between the Halden and BOR-60 specimens. This difference in the post-irradiation material strength cannot be explained by the dissimilar doses in the two irradiations. It is well known that irradiation hardening is an increasing function of the accumulated dose until saturation. The dose range for the comparison of the BOR-60 and Halden SSRT results is below or at the saturation dose. Therefore, the difference in the post-irradiation strength can only be attributed to the irradiation parameters other than accumulated dose.

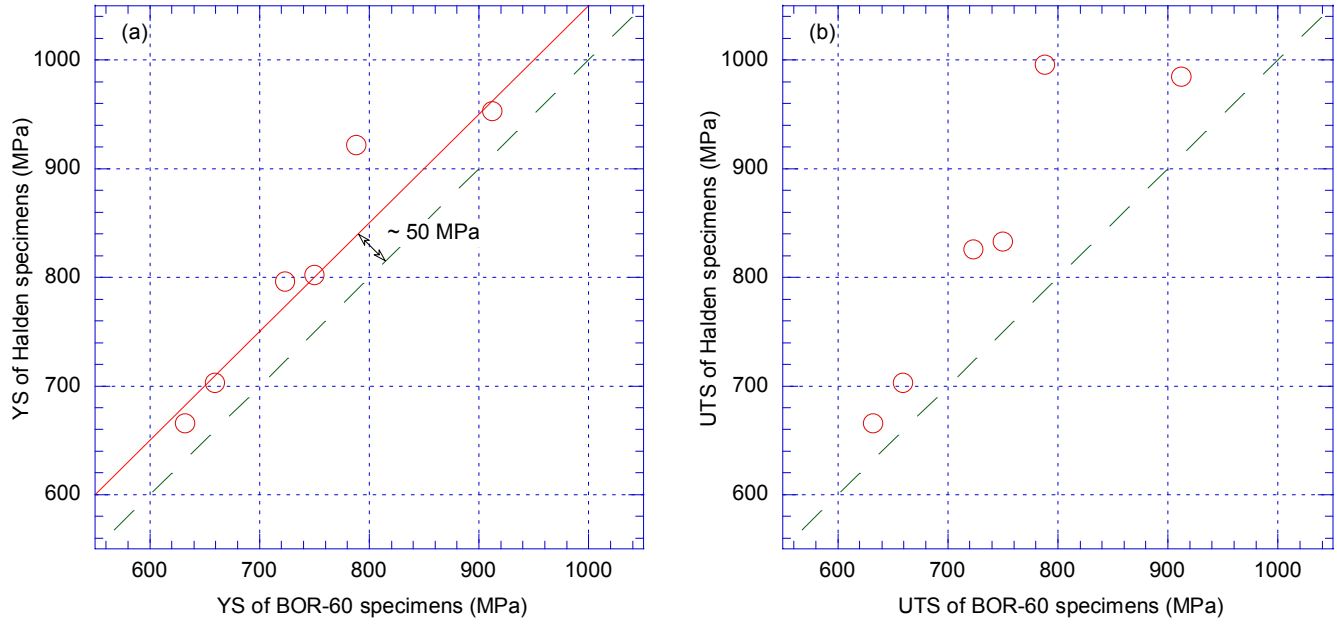

Figure 40. Results from SSRT tests in high-DO water on BOR-60 and Halden specimens: (a) YS and (b) UTS. (A 50 MPa increase in YS is shown by the red line.)

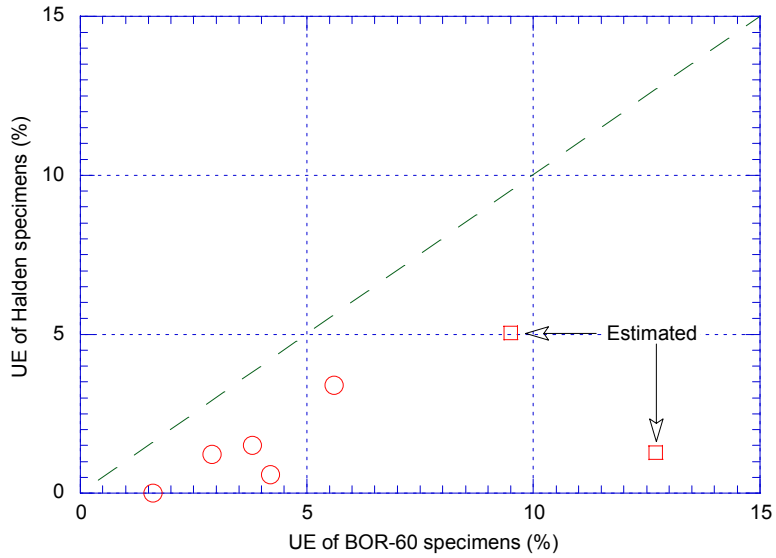

Figure 41.
Uniform elongation obtained from SSRT tests in high-DO water on BOR-60 and Halden specimens.

The Halden specimens underwent a dry irradiation in a heavy water reactor at ≈290°C, while the BOR-60 specimens were irradiated in a sodium-cooled fast breed reactor at ≈320°C. The two irradiations differed in irradiation environment, neutron spectrum, and irradiation temperature. It is known that decarburization could occur in SSs exposed to high temperature sodium. Consequently, the mechanical properties of SSs could be affected by sodium exposure. However, at the BOR-60 irradiation temperature (≈320°C), such effects are insignificant. The differences demonstrated by comparing the BOR-60 and Halden SSRT tests cannot be explained by sodium exposure.

It has been widely accepted that dpa is a fundamental damage parameter that characterizes the level of lattice displacement and can be correlated well with point defect production for a wide range of neutron spectra.[16] However, the level of lattice displacement does not contribute to the irradiation effects directly; instead, the survival point defects that are available for clustering and reacting with various sinks are responsible for the observable irradiation effects, such as irradiation hardening, radiation-induced segregation (RIS), and IASCC. Since the survival rate of point defects is sensitive to the nature of the displacement events, neutron flux and spectrum can influence the outcome of radiation damage. Given the two irradiations in this study, a lower damage rate and a softened neutron spectrum are expected for the Halden reactor. The relatively low damage rate and softened neutron spectrum can reduce the recombination rate of point defects.[16] The different neutron spectra in two irradiations could also lead to different helium production rates which in turn affect microstructure evaluation in specimens. With these mechanisms, irradiation effects resulting from the two irradiations can be different at the same dose level.[29,30]

Irradiation temperature may also be a contributor to the difference between the Halden and BOR-60 irradiations. The irradiation microstructure is a function of irradiation temperature.[30,31,32] The point-defect survival rate and the microstructural evaluation can be strongly affected by the irradiation temperature. For austenitic SSs, vacancies resulting from displacement damage become mobile at ≈300°C. As a result, the microstructural evolution becomes increasing sensitive to the irradiation temperature at this temperature range. It has been shown that, the density of large Frank loops increases gradually while the density of "black-dot" defects drops rapidly between 200°C and 300°C.[33] Consequently, a peak YS appears at ≈300°C for austenitic SSs.[34] The irradiation temperatures in this study fall in this sensitive range (≈290°C for the Halden irradiation and ≈320°C for the BOR-60 irradiation). So, despite many similarities between the two irradiations, it is understandable that the

higher irradiation temperature for BOR-60 specimens can result in a low post-irradiation strength in the SSRT tests.

4.1.2 IASCC Susceptibility Resulting from BOR-60 and Halden Irradiations

The IG area fractions (in percent) for the specimens from the Halden and BOR-60 irradiations are summarized in Table 6. Materials identified as both vulnerable and resistant to IASCC in the Halden project[19,20] were selected for the current study. For the Halden specimens, Heats C3, C9, and 945 showed a significant amount of IG cracking (>20%), while Heats C1, C12, L5 and 327 showed no or a minimal amount of IG morphology. For the BOR-60 specimens, two of the three susceptible materials (Heats C9 and 945) have large IG area fractions, and all the other alloys exhibited no IG cracking. As shown in Fig. 42, susceptibility to IASCC is consistent in both irradiations for most materials, except for the Type 304L SS from Heat C3. Also, for the IASCC susceptible materials (Heats C9 and 945), Heat C9 shows a larger IG fraction than Heat 945 in both irradiations. So, the degree of susceptibility seems also unaffected by different irradiations.

As shown in Fig. 42, more materials showed IG fracture morphology in the Halden irradiation than in the BOR-60 irradiation. For Heat C3, no IG crack occurred in the BOR-60 specimens, but quite a large IG area fraction was observed in the Halden specimens. Similarly, IG cracking is absent for Heats C12 and L5 in the BOR-60 irradiation, but IG cracks, although relatively small, are detected for the same heats in the Halden irradiation. Thus, the BOR-60 irradiation seems somewhat less effective in stimulating IG cracking for most materials tested in this study. The differences in the damage rate and irradiation temperature may be responsible for the observed difference in IASCC susceptibility in the two irradiations. The slightly lower strain rate in Halden SSRT tests may also contribute to the development of IG cracking in the Halden specimens.

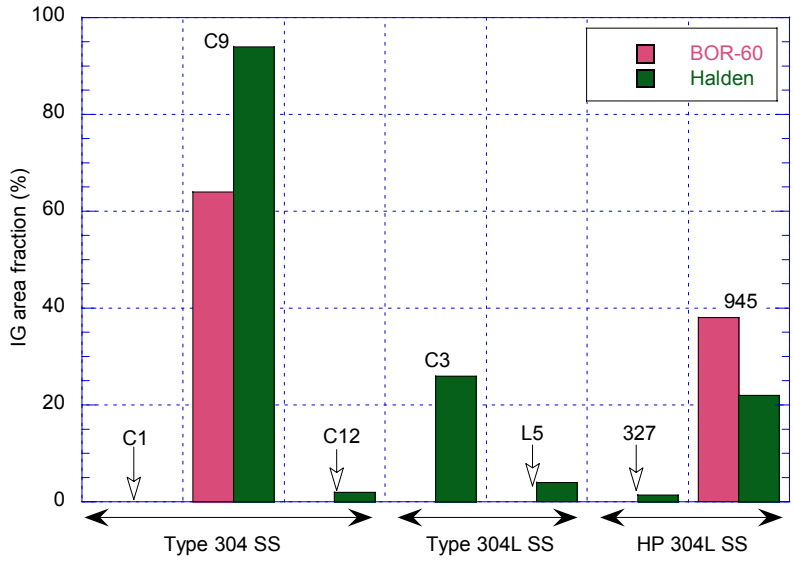

Figure 42.
IG area fraction in BOR-60 and Halden specimens tested in high-DO water at 289°C.

4.2 Irradiation Microstructure and Void Swelling for Selected BOR-60 Specimens

4.2.1 Irradiation Microstructure

The results from the TEM characterization on SSs and Alloy 690 irradiated in the BOR-60 reactor are summarized in Table 7. The main microstructural features observed in these irradiated SSs and Alloy 690 were the faulted Frank loops that lie on the {111} crystallographic planes with a Burger's vector of a/3<111>. The relrod imaging technique is well suited for the quantitative measurement for such irradiation defects in the austenitic structure.

Table 7. TEM characterization on SSs and Alloy 690 irradiated in the BOR-60 at ≈320°C to ≈25 dpa.

Material Type	Heat ID	Loop Size (nm)	Loop density (x 10^{22} m^{-3})	Voids
Type 304 SS, SA, low S	C12	25.5	3.0	No
Type 304 SS, SA, high S	C9	8.1	4.6	No
Type 304 SS from ABB, CW	2333CW	Not measured	Not measured	No
Type HP 304L SA, high O	945	12.2	1.2	No
Type 316 LN SA	623	5.8	1.7	No
Cast SS CF-3, 13.5% Ferrite	52	8.5	2.8	No
Cast SS CF-8 Cast SS, 13.5% Ferrite	59	7.7	3.1	No
Cast SS CF-8 Cast SS, 23.4% Ferrite	68	16.2	1.7	No
Alloy 690, base alloy	690 BASE	28.9	1.1	Yes
GBE Alloy 690	690 GBE	17.0	1.4	Yes

Five austenitic SSs were examined in this study. The Frank loop densities in these alloys were within the same order of magnitude, and the loop sizes varied from 25.5 nm in the low-S Type 304 SS to 5.8 nm in Type 316 LN SS. This result is consistent with the earlier literature data, in which a density of ≈9.2x10^{22} m^{-3} and an average size of 6.9 nm were reported for the Frank loops in a Type 316 SS baffle bolt irradiated in a commercial PWR at 320°C to 19.2 dpa[35] and a 6.2 x 10^{22} m^{-3} density and a 7.3 nm mean size were measured for the defects in a Type 304 SS an SA irradiated in the BOR-60 at 330°C to 20 dpa.[36]

Cast SSs consisting of both ferritic and austenitic phases have mixed characteristics and are frequently used in the main coolant pipes of PWRs. The microstructures of the materials were also dominated by a high density of Frank loops as shown in Table 7. The average size and density of Frank loops in Heat 52 are very close to those in Heat 59. It seems the dislocation structures were not altered with different carbon contents in Heats 52 and 59 respectively. The average loop size in Heat 68 is about twice of that in Heats 52 and 59, while the density is about half. According to Table 1, along with the different ferrite content percentages, the weight percentages of elements Ni, P, and S for Heat 68 are 8.08, 0.021, and 0.014, those for Heat 59 are 9.34, 0.008, and 0.007 respectively. These compositional differences may also contribute to the different irradiated dislocation microstructures between sample Heats 68 and 59 whose carbon contents are identical. Further study is needed to determine the effects of minor alloying elements on the evolution of irradiated microstructures.

The mean size and density of the dislocation loops in the irradiated nickel alloys are also summarized in Table 7. The average size of the Frank loops in heat base Alloy 690 is larger than that in GBE Alloy 690, while the loop density for the base alloy is slightly lower. Apparently, the

microstructure that resulted from the GBE processing affected the formation of defect structures after irradiation. The influence of GBE process is more pronounced on the loop size than on the density.

4.2.2 Void Swelling

Voids or cavities were examined for all TEM specimens using the through-focusing technique under high magnification. Within the resolution limits of the equipment, no voids were found for all austenitic and cast SSs, but a few voids were visible in the two Alloy 690 specimens. The absence of voids in the austenitic and cast SSs is consistent with the results that are summarized by Chung.[12]

The baffle-former plate in the core of a Westinghouse-designed PWR was examined earlier by others.[37,38,39] Void swelling data were obtained from TEM measurements performed on bolt heads and lock bars, on the shank, and on the threaded section. The bolt head temperature was expected to be near that of the reactor coolant water, while the bolt threads operated at a higher temperature because the reactor coolant dissipated less of the temperature increase caused by gamma heating. Table 8 lists the void swelling data and the corresponding conditions. The greatest swelling was found in the thread region, consistent with the higher irradiation temperature. The bolt heads and lock bars exhibited little or no voids, consistent with the observation that void formation is not expected to occur at or below 299ºC.

Table 8. Void swelling in PWR lock bars and baffle bolts

Specimen	Irr. Temp. (ºC)	Dose (dpa)	Swelling (%)
SA Type 304 SS lock bars	290	20	0.0
SA Type 347 SS bolt (threads)	333	8.6	0.029
SA Type 347 SS bolt (head)	290	16.4	0.0
SA Type 347 SS bolt (threads)	333	11	0.0009
SA Type 347 SS bolt (head)	290	14.1	0

In contrast, significant swelling was found in some pre-loaded components exposed to higher temperature. Edwards et al.[40] evaluated void swelling of the baffle-former bolts of Tihang 1 fabricated from a single heat of CW Type 316 SS. The baffle bolt was pre-loaded in a range between ~20 and 37.5 kN, and the irradiation conditions were between 320°C to 343°C and 8.7-19.2 dpa for different positions. The cavity characteristics are summarized in Table 9. The void swelling was determined from the cavity density and mean size. As the temperatures are higher at the shank and near the threads than those at the bolt head, the void swelling increased considerably, and the data show that void swelling at 320-343°C is insignificant at doses to roughly 20 dpa.

Table 9. Density and average size of loops and cavities for each position. [40]

Position (mm)	Dose (dpa)	Irradiation Temp. (°C)	Cavities		Swelling (%)
			Density (x $10^{20}m^{-3}$)	Average Size (nm)	
1	19.2	320	<1	<2	<0.01
25	13.2	343	0.61	8.6	0.20
55	8.7	333	1.0	7.7	0.24

The effect of the damage rate on the swelling was also examined by using PWR data available from two flux-thimble tubes irradiated in a Japanese PWR plant by Fujii et al.[41] These two tubes were

fabricated from 15% cold-worked Type 316 SS and installed in the fuel assemblies during PWR operation. One tube was exposed to neutrons for 9 effective full power years (EFPY) and the other one was exposed for 13 EFPYs. The specimens were taken from the active fuel region and also from above and below the fueled region. In this study, cavities were identified by means of a series of through-focus TEM images, and the thickness of the thin foil of specimen was evaluated by a stereomicroscopy technique. All the cavities were small and spherical, a characteristic feature for helium-filled bubbles. The swelling was calculated from the number density and diameter of the cavities, and it ranged from 0.015 to 0.042%. Table 10 summarizes the characterization of void size, distribution and void swelling. The data are consistent with the swelling data from PWRs reviewed in earlier sections, and the largest swelling observed was only 0.042% at 28 dpa dose, 6.9 x 10^{-8} dpa/s dose rate, and 320ºC. These data also show that the swelling depends on the combined effects of all these variables.

Table 10. Summary of cavity and swelling data in CW 316 irradiated in Japanese PWR plant [41]

Dose (dpa)	Dose Rate (dpa/s)	Temp. (ºC)	Average diameter (nm)	Density ($x10^{23}m^{-3}$)	Swelling (%)
1	$2.0x10^{-9}$	290	None	None	None
3	$8.0x10^{-9}$	290	0.94	3.6	0.015
10	$2.6x10^{-8}$	320	0.92	5.0	0.020
28	$6.9x10^{-8}$	320	0.95	9.4	0.042
31	$7.6x10^{-8}$	290	1.01	6.9	0.038
33	$8.2x10^{-8}$	320	1.04	3.1	0.018
53	$1.3x10^{-7}$	300	1.05	5.8	0.036
35	$1.1x10^{-7}$	310	0.94	3.8	0.016
35	$1.1x10^{-7}$	310	0.96	4.2	0.020
35	$1.1x10^{-7}$	310	0.98	3.8	0.019

At the EOL of PWRs, the dose can approach 100 dpa and the irradiation temperature can reach 370º C in thick sections due to gamma heating. Austenitic materials irradiated in PWRs under these conditions are not readily available. Void swelling data from other irradiation sources relevant to the PWR have also been explored. Allen et al.[42] evaluated swelling in Type 304 SS irradiated at low dose rate in ERB-II following shutdown. The peak displacement rate was approximately 6.5 x 10^{-8} dpa/s, and the irradiation temperature varied from 371 to 390º C. The data are summarized in Table 11, and the maximum swelling is 1.3%. The swelling rate is about 0.1%/dpa in these materials and is still at an early stage within the transient portion of a swelling versus dose curve.

Table 11. Void swelling of Type 304 SS in ERB-II. [42]

Sample	Reactor Grid Position	Dose Rate (dpa/s) in Grid Position	Total Dose (dpa)	Average Temp (°C)	Average Void Diameter (nm)	Swelling (%)
Refl Row 14	8F4 14E10	$2.9x10^{-7}$ $1.5x10^{-8}$	10	379	15.7	1.3
Refl Row 10	10C2	$4.7x10^{-8}$	12.2	378	10.8	0.3
SURV row 12 K-5	12E8	$3.1x10^{-8}$	8.9	375	11.5	0.7

The finding of no detectable voids in the BOR-60 austenitic SSs irradiated to ≈25 dpa may be attributed to the relatively high damage rate (≈10^{-6} dpa/s) and low irradiation temperature (≈320°C). As evident from the literature review, a longer incubation period may be needed for irradiations at high dose rate and low temperature. The lack of void swelling for austenitic SSs at ≈25 dpa in our study does not

clarify the problem of the void swelling in some PWR components. Further study is needed for specimens with higher doses.

For Alloy 690, voids were observed in the GBE and base materials in our study. The voids were scattered unevenly, and most of them paired with precipitates or were located at the grain boundaries. Based on the TEM images of these two samples, the base Alloy 690 had fewer voids than the material with the GBE treatment. Nonetheless, it is easier to form voids in Alloy 690 than in austenitic SSs under the same irradiation condition. This result is consistent with other studies on Ni-based alloys.

The void swelling in nickel and its alloys has been studied under ion, electron, and neutron irradiations.[43-49] All these experimental studies resulted in some void swelling at varied levels. For pure nickel irradiated with neutrons at 300°C (573 K), even to a dose of 0.40 dpa, voids appear with a size around 10 nm.[43] The microstructural evolution in Inconel 718 was also investigated using 3.5 MeV Fe^+, 370 KeV He^+, and 180 KeV H^+ either singly or simultaneously at 200°C (473 K). Cavities were observed with a mean size of 1.0 nm in tests at a high density with a dose as low as 0.01 dpa for Fe^++He^++H^+ irradiation[44]. In a study on the influence of temperature, voids were also observed in neutron irradiated Ni alloys at 260-420°C (533-693 K) and 0.46 dpa.[45] For an austenitic high-nickel alloy irradiated in BOR-60 at temperatures between 320 and 570°C, up to 5% swelling was observed in the material[46]. For the irradiation at high temperature, swelling slightly decreased with increasing Ni content due to the influence of Ni on incubation dose; however, for the temperature range of 300-325°C (573-598 K), this dominant Ni influence was not reported.

5 Summary

The SSRT tests were conducted on BOR-60 specimens in air and in high-DO water. By comparing identical materials irradiated in the BOR-60 and Halden reactors to a similar dose, the influence of irradiation conditions on the SSRT properties and IASCC susceptibility was investigated. Additionally, TEM microstructural characterization was carried out on selected BOR-60 specimens irradiated to ≈25 dpa. The main conclusions of this preliminary study are as follow:

(1) The SSRT tests in high-DO water produced similar results among the different materials irradiated in both Halden and BOR-60 reactors. However, the post-irradiation strengths (YS and UTS) for the BOR-60 specimens were consistently lower than those of the corresponding Halden specimens. The BOR-60 specimens also elongated more than their Halden counterparts.

(2) The IG cracking behavior resulting from the high-DO water tests for most of the tested materials was consistent in both the Halden and BOR-60 irradiations. Nonetheless, the BOR-60 irradiation was somewhat less effective in stimulating IASCC among the tested materials.

(3) All the irradiated microstructures at ≈320°C and ≈25 dpa were dominated by a high density of Frank loops, which varied in mean size and density for different alloys. No voids were observed by TEM of irradiated austenitic SSs and cast SSs, while a few voids were found in the base and GBE Alloy 690. It appears that void swelling is negligible for the SS specimens at this temperature and dose level.

References

1. Berge, Ph., and F. de Keroulas, "The Present Situation Regarding Environmental Degradation of Components in Pressurized Water Reactors," Proc. 4th Int. Symp. on Environmental Degradation of Materials in Nuclear Power Systems - Water Reactors, NACE, Houston, TX, pp. 1-11, 1990.

2. Andresen, P. L., F. P. Ford, S. M. Murphy, and J. M. Perks, "State of Knowledge of Radiation Effects on Environmental Cracking in Light Water Reactor Core Materials," Proc. 4th Intl. Symp. on Environmental Degradation of Materials in Nuclear Power Systems - Water Reactors, NACE, Houston, TX, pp. 1.83-1.121, 1990.

3. Cheng, Craig F., "Intergranular Stress-Assisted Corrosion Cracking of Austenitic Alloys in Water-Cooled Nuclear Reactors", J. Nucl. Mater., 56, 11-33, 1975.

4. Garzarolli, F., D. Alter, and P. Dewes, "Deformability of Austenitic Stainless Steels and Nickel-Base Alloys in the Core of a Boiling and a Pressurized Water Reactor," Proc. Intl. Symp. on Environmental Degradation of Materials in Nuclear Power Systems - Water Reactors, American Nuclear Society, La Grange Park, IL, pp. 131-138, 1986.

5. Scott, P., "A Review of Irradiation Assisted Stress Corrosion Cracking", J. Nucl. Mater., 211, 101-122, 1994.

6. Garzarolli, F., H. Rubel, and E. Steinberg, "Behavior of Water Reactor Core Materials with Respect to Corrosion Attack," Proc. Intl. Symp. on Environmental Degradation of Materials in Nuclear Power Systems - Water Reactors, NACE, Houston, TX, pp. 1-24, 1984.

7. Garner, F. A., "Irradiation Performance of Cladding and Structural Steels in Liquid Metal Reactors," *Materials Science and Technology - A Comprehensive Treatment*, R. W. Cahn, P. Haasen, and E. J. Kramer, eds., VCH Publishers Inc., New York, 1994.

8. Garner, F. A., "Recent Insights on the Swelling and Creep of Irradiated Austenitic Alloys", J. Nucl. Mater., 122&123, 459-471, 1984

9. Mansur, L. K., "Theory and Experimental Background on Dimensional Changes in Irradiated Alloys," J. Nucl. Mater. 216, 97-123, 1994.

10. Garner, F. A., and M. B. Toloczko, "Irradiation Creep and Void Swelling of Austenitic Stainless Steels at Low Displacement Rates in Light Water Energy Systems," J. Nucl. Mater. 251, 252-261, 1997.

11. Porollo, S. I., Yu. V. Konobeev, A. M. Dvoriashin, V. M. Krigan, and F. A. Garner, "Determination of the Low Temperature Limit of Void Swelling of Stainless Steels at PWR-relevant Displacement Rates," Proc. 10th Intl. Symp. on Environmental Degradation of Materials in Nuclear Power Systems - Water Reactors, NACE, Houston, TX, 2002.

12. Chung, H. M., "Assessment of Void Swelling in Austenitic Stainless Steel Core Internals," NUREG/CR-6897, ANL-04/28, Jan. 2006.

13. Garner, F. A., L. R. Greenwood and D. L. Harrod, "Potential High Fluence Response of Pressure Vessel Internals Constructed from Austenitic Steels," Proc. 6th Intl. Symp. on Environmental Degradation of Materials in Nuclear Power Systems - Water Reactors, TMS, Warrendale, PA, 1993.

14. Was, G. S. and P. L. Andresen, "Stress Corrosion Cracking Behavior of Alloys in Aggressive Nuclear Reactor Core Environments," Corrosion, 63 (1), 19-45, 2007.

15. Robinson, M. T., "Basic Physics of Radiation Damage Production," J. Nucl. Mater. 216, 1-28, 1994

16. Greenwood, L. R., "Neutron Interactions and Atomic Recoil Spectra," J. Nucl. Mater. 216,.29-44, 1994

17. Norgett, M. J., M. T. Robinson, and I. M. Torrens, "A Proposed Method of Calculating Displacement Dose Rates,"Nucl. Eng. Des. 33, 50-54, 1975

18. Electric Power Research Institute, "CIR II Program: Description of the Boris 6 Experiment in the BOR-60 Fast Breeder Reactor," Report No. 1009418, Palo Alto, CA, 2004.

19. Chen, Y., O. K. Chopra, W. K. Soppet, N. L. Dietz Rago, and W. J. Shack, "Irradiation-Assisted Stress Corrosion Cracking of Austenitic Stainless Steels and Alloy 690 from Halden Phase-II Irradiation," NUREG/CR-6965, ANL-07/11, 2008.

20. Chung, H. M. and W. J. Shack, "Irradiation-Assisted Stress Corrosion Cracking Behavior of Austenitic Stainless Steels Applicable to LWR Core Internals," NUREG/CR-6892, ANL-04/10, Jan. 2006.

21. Alexander, D. J., J. E. Pawel, L. M. Grossbeck, A. F. Rowcliffe, and K. Shiba, "Fracture Toughness of Irradiated Candidate Materials for ITER First Wall/Blanket Structures," Effect of Radiation on Materials: 17th Intl. Symp., ASTM STP 1270, American Society of Testing and Materials, Philadelphia, PA, pp. 945–970, 1996.

22. Mills, W. J., "Fracture Toughness of Irradiated Stainless Steel Alloys," Nucl. Technol., 82 (3), 290–303, 1988.

23. Sindelar, R. L., G. R. Caskey, Jr., J. K. Thomas, J. R. Hawthorne, A. L. Hiser, R. A. Lott, J. A. Begley, and R. P. Shogan, "Mechanical Properties of 1950s Vintage Type 304 Stainless Steel Weldment Components after Low Temperature Neutron Irradiation," 16th Intl. Symp. on Effects of Radiation on Materials, ASTM STP 1175, American Society of Testing and Materials, Philadelphia, PA, pp. 714–746, 1993.

24. Lucas, G. E., "The Evolution of Mechanical Property Change in Irradiated Austenitic Stainless Steels," J. Nucl. Mater., 206, 287-305, 1993.

25. Garner, F. A., "Irradiation Performance of Cladding and Structural Steels in Liquid Metal Reactors", Materials Science and Technology – A Comprehensive Treatment, Ed. R. W. Cahn, P. Haasen, E. J. Kramer, Vol. 10A, Part I, Volume Ed. by B. R. T. Frost, VCH Publishers Inc., New York, NY, 1994, pp.420.

26. Zinkle, S. J., P. J. Maziasz and R. E. Stoller, “Dose dependence of the microstructural evolution in neutron-irradiated austenitic stainless steel”, J. Nucl. Mater., 206, pp. 266-286, 1993

27. Maziasz, P. J., “Overview of microstructural evolution in neutron-irradiated anstenitic stainless steels”, J. Nucl. Mater., 205, pp.118-145, 1993

28. Edwards, D. J., E. P. Simonen and S. M. Bruemmer, “Evolution of fine-scale defects in stainless steels neutron-irradiated at 275°C”, J. Nucl. Mater., 317, pp.13-31, 2003

29. Brager, H. R., L. D., Blackburn, and D. L. Greenslade, “The dependence on displacement rate of radiation-induced changes in microstructure and tensile properties of ASIS 304 and 316”, J. Nucl. Mater., 122&123, pp. 332-337, 1984

30. Garner, F. A., “Evolution of microstructure in face-centered cubic metals during irradiation”, J. Nucl. Mater., 205, pp.98-117, 1993

31. Zinkle, S. J., P. J. Maziasz and R. E. Stoller, “Dose dependence of the microstructural evolution in neutron-irradiated austenitic stainless steel”, J. Nucl. Mater., 206, pp.266-286, 1993

32. Maziasz, P. J., “Overview of microstructural evolution in neutron-irradiated austenitic stainless steels”, J. Nucl. Mater., 205, pp.118-145, 1993

33. Maziasz, P. J., “”, J. Nucl. Mater., 191-194, pp.701, 1992

34. Lucas, G. E., “The evolution of mechanical property change in irradiated austenitic stainless steels”, J. Nucl. Mater., 206, pp.287-305, 1993

35. Van Duysen, J. C., J. Bourgoin, C. Janot, and J.M. Penisson, “Evolution of the microstructure of PWR pressure vessel steels from the CHOOZ. A reactor surveillance program after long-term irradiations”, STM Special Technical Publication, Effects of Radiation on Materials: 15th International Symposium, pp.117-130, 1992

36. Yang, W.J.S, H.R. Brager and F.A. Garner, “Radiation-induced phase development in AISI 316”, Phase Stab. Irr., Proc. Symp., pp.257-269, 1980

37. Byrne, S, F. A. Garner, S. Fyfitch and Ian L. W. Wilson, “Application of void swelling data to evaluation of pressurized water reactor components”, Proc. 10th Intl. Conf. on Environmental Degradation of Materials in Nuclear Power Systems-Water Reactors, NACE/ANS/TMS, Aug.5-9, 2001

38. Garner, F. A., B. M. Oliver, L. R. Greenwood, D. J. Edwards and S. M. Bruemmer, “Generation and retention of helium and hydrogen in austenitic steels irradiated in a variety of LWR and test reactor spectral environments”, Proc. 10th Intl. Conf. on Environmental Degradation of Materials in Nuclear Power Systems-Water Reactors, NACE/ANS/TMS, Aug.5-9, 2001

39. Edwards, D. J., F. A. Garner, B. A. Oliver and S. M. Bruemmer, “Microstructural evaluation of a cold-worked 316ss baffle bolt irradiated in a commercial PWR”, Proc. 10th Intl. Conf. on Environmental Degradation of Materials in Nuclear Power Systems-Water Reactors, NACE/ANS/TMS, Aug.5-9, 2001

40. Edwards, D. J., F.A. Garner, B.A. Oliver and S.M. Bruemmer, Proc. 10th Intl. Conf. on Environmental Degradation of Materials in Nuclear Power Systems-Water Reactors, NACE/ANS/TMS, Aug.5-9, 2001

41. Fujii, K., K. Fukuya, G. Furutani, T. Torimaru, A. Kohyama and Y. Katoh, Proc. 10th Intl. Conf. on Environmental Degradation of Materials in Nuclear Power Systems-Water Reactors, NACE/ANS/TMS, Aug.5-9, 2001

42. Allen, T. R., H. Tsai, R. S. Daum, D. L. Porter, J. I. Cole, T. Yoshitake, N. Akasaka, T. Donomae,S. Mizuta, J. Ohta, K. Dohi, and H. Kusanagi, Proc. 11th Intl. Conf. on Environmental Degradation of Materials in Nuclear Power Systems - Water Reactors, Aug. 10-14, 2003

43. Yoshiie, T., T. Ishizaki, Q. Xu, Y. Saoh, M. Kiritani, J. Nucl. Mater. 307-311 (2002) 924

44. Hashimoto, N., J.D. Humn, T.S. Byun and L.K. Mansur, J. Nucl. Mater. 318 (2003) 300

45. Xu, Q., and T.Yoshiie, J. Nucl. Mater. 307-311 (2002) 380

46. Shamardin, V. K., V.S. Neustroev, A.V. Povstyanko, T.M. Bulanova, Z.E. Ostrovsky,; A.A. Kuznetzov, I. P. Kursevitch, V.A. Nikolaev, ASTM Special Technical Publication (1996), STP 1270(Effects of Radiation on Materials: 17th International Symposium, 1994), 842

47. James, F. S., and F.A. Garner, ASTM Special Technical Publication (1996), STP 1270(Effects of Radiation on Materials: 17th International Symposium, 1994), 1039

48. Porollo, S. I., A.M. Dvoriashin, A.N. Vorobjev, Yu.V. Konobeev, V.M. Krigan, E.G. Mironova, N.I. Budylkin and F.A.Garner, J. Nucl. Mater. 283-287 (2000) 239

49. Yamakawa, K., and Y.Shimomura, J. Nucl. Mater. 264 (1999) 319

Nuclear Engineering Division
Argonne National Laboratory
9700 South Cass Avenue, Bldg. 212
Argonne, IL 60439-4838

www.anl.gov